University of Bergen

Faculty of Mathematics and Natural Sciences

Master thesis in meteorology and oceanography, with specialization in physical oceanography

Lofoten eddies observed by Seagliders

Author
Hauk Løvseth

Supervisors
Prof. Ilker Fer
Dr. Anthony Bosse

October 12, 2018

Abstract

When the Norwegian Atlantic Current passes the Lofoten Basin, it loses a large amount of mass and heat to mesoscale eddies as a result of instabilities of the mean current along the Norwegian Slope. The eddies subsequently propagate into the interior of the Lofoten Basin, where they are trapped by the topography, making the basin the most energetic with the largest pool of Atlantic Water in the Nordic Seas. Observational studies have been limited, mainly to surface signature inferred from remote sensing data. This study investigates mesoscale eddies in the Lofoten Basin using Seaglider observations taken from 2012 to 2017 and an altimetry-derived dataset that characterizes eddies based on the surface signature. Nine anticyclones and two cyclones have been characterized using Seaglider data. Eddies in the basin have a mean radius and velocity maximum of 19 km and $0.4\,\mathrm{m\,s^{-1}}$. The Anticyclones have a mean anomalous heat content, available potential energy and eddy kinetic energy of 14.0×10^{18} J, 15×10^{13} J and 9×10^{13} J. Cyclones of -8×10^{18} J, 10×10^{13} J and 14×10^{13} J. The slope branch of the Norwegian Atlantic Current have been identified as the source region, and a freshening of anticyclones in the observation period was observed. The altimetry-derived dataset showed a pattern of eddies being generated along the continental slope on the eastern border of the basin and moving in a cyclonic pattern around the basin. The number of eddies required to balance wintertime heat loss from the basin was found to be 28 to 37.

Acknowledgments

Til veiladerane mine, Ilker og Anthony, vil eg gjerne sei tusen takk for tålmodig og konstruktiv veiledning. Eg vil og takke Roshin P. Raj på nansen senteret for å produsere altimetri datasettet eg har brukt i oppgåva.

Alle venane mine på gfi vil eg takke for dei siste fem åra. Og tusen takk til Synnøve for å holde meg nogenlunde med god psykisk og fysisk helse dei siste månadane. Mor og far vil eg takke for at eg finst, og til været vil eg rette ein utakk for alle monge solskinnsdagane tilbrakt innandørs med Matlab. Og til slutt, Lofoten Bassenget, takk for du er så full av virvlar, oppgåva hadde ikkje vore den same utan deg.

Contents

1 Introduction

This study investigates mesoscale eddies in the Lofoten Basin using hydrographical observations from Seagliders and a satellite altimetry-derived product which tracks and characterizes eddies.

The Lofoten Basin is a topographic depression in the Norwegian Sea, situated west of the Lofoten Islands. The Lofoten Basin stand out in an oceanographic context by the presence of a thick Atlantic Water layer and considerable eddy activity. The layer of warm and salty Atlantic Water in the Lofoten Basin reaches depths larger than 700 m (*Bosse* et al. 2018) and the basin's heat and salt contents are higher than other ocean basins in the Nordic Seas (*Rossby* et al. 2009). The abundance of warm water leads to a substantial wintertime heat loss. Even though the Lofoten basin only constitutes a surface area equal to one-fifth of the Nordic Seas, it is responsible for one-third of the buoyancy loss (*Richards* et al. 2015).

The source for this large heat and salt anomaly is shown to be Atlantis Water eddies shedding from the Norwegian Atlantic Slope Current that propagate into the basin. Instabilities generate eddies as the current flows east of the Lofoten and Vesterålen Islands. This process is documented using drifters (e.g. *Koszalka* et al. 2011; *Rossby T.* et al. 2009), altimetry (e.g. *Raj* et al. 2016a) and models (e.g. *Isachsen* et al. 2012; *Köhl* 2007). As a consequence, the greatest heat loss undergone by the Norwegian Atlantic Slope Current takes place as it passes the Lofoten Basin (*Isachsen* et al. 2012). Estimates suggest that more than one third of the slope current is required to be ejected inform of eddies and transported into the basin to sustain the warm water layer in the basin (*Rossby* et al. 2009). This is a substantial mass and heat loss from a current essential for the global transport of warm water into the Arctic; one of the areas most influenced by climate change (*Carmack* et al. 2015).

There are not many studies that characterize eddies in Lofoten Basin using in-situ hydrographical observations. Recently, several hydrographic studies focused on the "Lofoten Basin Eddy" (e.g. *Yu* et al. 2017; *Fer* et al. 2018; *Søiland* et al. 2016), a permanent eddy that resides in the deepest part of the basin. But the properties of the general eddy field in the Lofoten Basin are less investigated. Studies abut the eddies in the Lofoten Basin are typically from satellite altimetry (e.g *Raj* et al. 2016a) or numerical modeling (e.g, *Volkov* et al. 2013). A notable exception using in-situ observations is a mooring based study that characterized anticyclones in the basin at a fixed location (*Richards* et al. 2015). Other hydrographic descriptions of eddies have been opportunistic. Cyclones in the basin remain to be investigated, even though altimetry shows that they are almost as prominent as anticyclones (*Raj* et al. 2016a).

How eddies distribute the energy drained from the slope current around the basin, is not

well known. There are few direct observations of eddies propagating into the deepest part of the basin, where they are believed to feed the Lofoten Basin Eddy with their energy by merging (*Raj* et al. 2015). The exact pattern of energy deposition by eddies remains elusive, but it is known that they spiral the basin following a cyclonic path (*Volkov* et al. 2013). The energy content of eddies in the Lofoten Basin, excluding the Lofoten Basin Eddy, has also not been thoroughly investigated.

The goal of this study is to improve the knowledge about the properties of eddies and their distribution in the Lofoten Basin. The main focus is put on anticyclones since they are the conduits of energy transfer from the Norwegian Atlantic Current, but cyclones are also characterized. The data set includes 8 Seaglider missions, deployed from July 2012 to May 2017, and a satellite altimetry derived eddy product. Seagliders are an autonomous underwater vehicle measuring oceanographic properties, and glides through the ocean, propelled by changes in their buoyancy. The eddy product gives the location and characteristics of cyclones and anticyclones deduced from sea surface height, in the period, from January 1993 to May 2017. The Gimsøy Section, a repeated hydrographic section across the slope current and into the basin taken from ships is also used.

The backbone of the study is the analysis to locate eddies in the Seaglider data and find their hydrographical and kinematic structure, energy content and dynamic properties. The satellite eddy product is used to investigate eddy propagation and statistical characteristics of the eddy field. The two data sets are combined to better understand how energy from the slope current is distributed in the basin.

The rest of this study is organized in four sections: In the "Background", I present the relevant basic theory that is applied in the study, elaborate on the oceanographic context of the Lofoten Basin and review earlier relevant studies. In "Methods and data" I present the data and the methods applied. Subsequently, results are presented giving a detailed description of an anticyclone, summary of all eddies analyzed, followed by the results for two cyclones. In "Discussion", I combine the results with the present knowledge of the basin and discuss the possible source locations for eddies, interannual variability, and the importance of eddies in the heat budget of the basin. In "Conclusion", I give a summary of the most important findings.

2 | Background

2.1 THEORETICAL BASIS

In this section, the basic theory relevant for the thesis is outlined. Most of the section is based on the textbook by *Cushman-Roisin* et al. (2011). When other sources are used they will be referenced to. We adopt the standard right-handed coordinate system with positive x and y is directed toward east and north and z positive upward.

2.1.1 The rotating earth

Ocean is a mass of fluid on a planet that rotates around it own axis at a frequency of $\Omega = 7.3 \times 10^{-5}\,\mathrm{rad\,s^{-1}}$. From the point of view of our every day life this rotation is not apparent, But its effect on the atmosphere and the ocean is fundamental. The effect of rotation on fluid motion varies with latitude, from no influence at equator to a maximum at the poles. The effect of rotation is expressed in the equations of fluid motion by the Coriolis parameter (f):

$$f = 2\Omega sin\theta, \tag{2.1}$$

where θ is the latitude. The rotation of the Earth diverts mass movement to the right in the northern hemisphere and to the left in the southern, effectively changing the sign of f. In the following we assume that we are on the northern hemisphere. Often one make the assumption that we are on a f-plane, meaning that the latitudal variations are so small that the variation of the Coriolis parameter is unimportant. Then the Coriolis parameter is assumed constant, $f = f_0 = 2\Omega sin(\theta_0)$. When taking into account the latitudinal variation of the Coriolis parameter, we operate on a β-plane. The Coriolis parameter on the β-plane is the first two terms of a Taylor expansion of f:

$$f = f_0 + \beta_o y, \tag{2.2}$$

where $f_0 = 2\Omega sin(\theta_0)$, $\beta_0 = 2\left(\frac{\Omega}{a} cos(\theta_0) l\right)$, θ_0 is the reference latitude, a is the radius of the Earth, and y is the deviation in north-south direction from the reference latitude.

2.1.2 The Rossby number and geostrophic balance

The importance of rotation on fluid motion scales as the speed of motion over a relevant length scale and the local rotation rate. This leads to a non dimensional number known as the Rossby

number:

$$Ro = \frac{U}{fL}, \tag{2.3}$$

where f is the Coriolis frequency, L the relevant length scale and U the speed of motion. When $Ro \ll 1$, planetary rotation dominates the flow. When $Ro \approx 1$, there is a balance between rotation and advection of mass. When $Ro \gg 1$, advection and small scale processes dominate.

At scales where $Ro \ll 1$, ocean currents are in a balance between the pressure and the Coriolis forces, known as the geostrophic balance. In this case, geostrophic horizontal velocities are given as:

$$u_g = -\frac{1}{\rho_0 f}\frac{\partial p}{\partial y}\,, \qquad v_g = \frac{1}{\rho_0 f}\frac{\partial p}{\partial x}, \tag{2.4}$$

where p is pressure and, ρ_0 is a reference density for the fluid. The pressure force works opposite to the gradient - from high to low pressure. A flow in strictly geostrophic balance flows along lines of constant pressure with higher pressure to right.

2.1.3 Effect of stratification

Ocean is a stratified fluid. When stratification is stable, density increases with depth. The buoyancy frequency (N) is the oscillation frequency of a vertical displaced fluid parcel in a stratified water column, $N^2 = \frac{-g}{\rho_0}\frac{\partial \rho}{\partial z}$. Where ρ is the density of the water column and g is the gravity constant.

The Froude number (Fr) is a measurement of the importance of stratification in the flow. It is given by the speed of motion (U) over the stratification frequency and the vertical scale of the fluid motion (H).

$$Fr = \frac{U}{NH}, \tag{2.5}$$

If $Fr \gtrsim 1$ stratification effects are important. Importance of stratification increases for decreasing Fr. This leads us to the Burger number (Bu), which is the squared ratio of the Rossby number to the Froude number:

$$\mathrm{Bu} = \left(\frac{\mathrm{Ro}}{\mathrm{Fr}}\right)^2 = \left(\frac{NH}{fL}\right)^2, \tag{2.6}$$

The Burger number expresses the ratio between the vertical stratification and the Earth‘s rotation. When $\mathrm{Bu} \sim 1$ rotation and stratification are equally important. For high Burger numbers, the flow is dominated by stratification and for low values, by rotation.

When $\mathrm{Bu} = 1$, the Froude number equals the Rossby number. In this case, solving equation (2.6) for L gives rise to a special length scale, the internal radius of deformation (L):

$$L = \frac{NH}{f}, \tag{2.7}$$

which is the length scale where rotation and stratification are equally important.

Another important concept for rotating stratified flow is thermal wind. This shows how the vertical shear of a flow in geostrophic balance is influenced by horizontal gradients of density:

$$\frac{\partial v}{\partial z} = -\frac{g}{\rho_o f}\frac{\partial \rho}{\partial x}, \qquad \frac{\partial u}{\partial z} = +\frac{g}{\rho_o f}\frac{\partial \rho}{\partial y} \tag{2.8}$$

When there is a horizontal gradient of density it creates a vertical velocity shear that is perpendicular to the gradient. The geostrophic shear will result in an increased velocity in depth to the direction that has denser water to the right.

2.1.4 Potential vorticity

The vorticity of a two dimensional flow is defined as: $\zeta = \frac{\partial v}{\partial x} - \frac{\partial u}{\partial y}$. $f + \zeta$ give the total vorticity of a fluid parcel. When total vorticity is divided by the height of the fluid parcel, we get potential vorticity,$q = \frac{f+\zeta}{H}$. It can be shown that potential vorticity is conserved for inviscid and homogeneous fluid that is not subjected to outside torque:

$$\frac{d}{dt}\left(\frac{f+\zeta}{H}\right) = 0 \tag{2.9}$$

As a consecuence, a fluid parcel that is stretched (increasing H), will have to balance this by an increase in vorticity or move nortward to increase f.

2.1.5 Sub-mesoscale and mesoscale flow

Processes in the ocean occurs on all scales, from the interaction of molecules to the global overturning of the oceans over thousands of years. Mesoscale is between these extremes. A typical length and timescale of mesoscale variability is from tens to hundreds of kilometers and from a few days to several months. Sub-mesoscale variability is typically on the length scale of one to ten kilometers. In a mesoscale flow Ro $\ll 1$, the flow is mostly controlled by rotation. For a sub-mesoscale flow Ro is in the order of one and non-linear processes and advection dominates (*Talley* et al. 2011).

2.1.6 Dynamics of eddies

An oceanic eddy is a rotating body of water that has anomalous temperature and salinity relative to its surroundings and a much shorter turnaround time than the timescale of the evolution of the embedded water mass. An eddy is classified either as a cyclone or an anticyclone. A cyclone rotates in the same direction as the Earth. In the northern hemisphere, this rotation is counter-clockwise, with positive vorticity. An anticyclone rotates in the direction opposite of the Earth - clockwise in the northern hemisphere, with negative vorticity.

On the f-plane ocean eddies are in balance between Coriolis, pressure and the centrifugal force - called the gradient wind balance. In cylindrical coordinates with origin set to the center of the rotation, the gradient wind balance is:

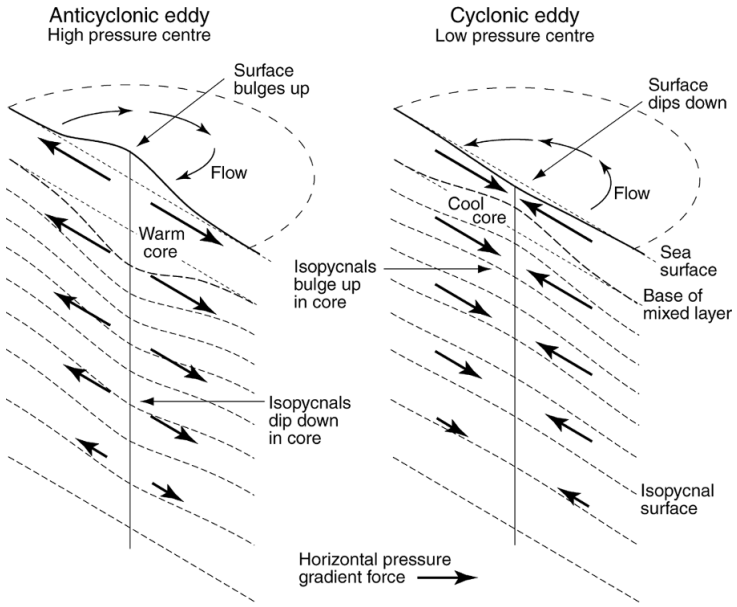

Figure 2.1 – Example of a warm core anticlonic eddy and a cold core cyclonic eddy. Arrows at depth indicate the pressure force, dotted lines are the isopycnals that increase with depth, arrows at surface indicate flow direction. Figure from *Robinson* (2010)

$$-\frac{v^2}{r} - fv = -\frac{1}{\rho_0}\frac{\partial p}{\partial r}, \tag{2.10}$$

where v is the azimuthal velocity, r is radial distance and p pressure. The first term on the left hand side is the centrifugal force, the second term is the Coriolis force, and on the right side is the pressure gradient. The centrifugal force is always directed outward while the Coriolis and pressure forces may change direction. The Coriolis force is directed inwards for anticyclones and outwards for cyclones, as a consequence cyclones need a low pressure in their center to achieve a balance of forces.

A scale analysis shows that in cases with a very small Rossby number, Ro $\ll 1$, the first term is negligible, giving mesoscale eddies in geostrophic balance. It can also be shown that in the cases with Ro $\gg 1$ and assuming that the pressure difference is a result of a density anomaly, the length scale of the eddy is much smaller than the radius of deformation: these are submesocale eddies.

In eddies at scales of the order of the internal deformation radius, the centrifugal force is comparable with the Coriolis force. The relative importance of the centrifugal force increases as the radius decreases. In eddies with a radius much smaller than the internal radius of deformation, $r \ll L$, the Coriolis force is negligible. At this scale a high pressure vortex cannot exist and the direction of rotation is not important. For an anticyclone with a high pressure core, the minimum possible radius is $r^2 \geq \frac{8\Delta p}{\rho_o f^2}$, below this radius eddies with a high pressure center cannot exist.

Figure 2.1 shows a vertical slice through examples of a cyclonic and an anticyclonic eddy in geostrophic balance. The anticyclone has a warm core and a local maximum of sea surface height in the center of rotation. The pressure force induced by the sloped sea surface point outward and

is balanced by the Coriolis force that point inward toward the center perpendicular to the flow that flows clockwise around the center. The pressure gradient induced by the raised sea surface lessens with depth since the density of the surrounding water mass is greater than the density inside the eddy. The lessening of the pressure gradient results in a decrease of velocity with depth - an effect of the thermal wind. The isopycnals flattens out with depth, and eventually the velocity and isopycnal signal of the eddy disappears. For the cyclonic eddy the sea surface dips down and the isopycnals rise toward the center. The pressure gradient is pointed inwards and the flow is cyclonic with the Coriolis force directed outward. The flow decreases in depth with thermal wind, as for the anticyclone.

As a consequence of potential vorticity, movements of eddies on the $-plane$ is a function of the ambient flow in the layer surrounding the eddy and the thickness gradient of this layer. An eddy will follow the flow that surrounds it, and in the presence of a layer thickness gradient, the propagation gets a velocity component perpendicular to the gradient with decreasing thickness to the right. In the absence of an ambient flow, this will cause eddies to move along lines of constant layer height. On the beta-plane the increase of the Coriolis parameter with latitude has a similar effect as the decrease of layer height to the north, causing a westward propagation of eddies.

2.1.7 The role of eddies in the ocean

In the ocean eddies, are an important carrier of water masses, as oceanic water can be trapped in an eddy at one point and be transported along vast distances. Mass transport by eddies is comparable to the transport of the global current and wind driven systems (*Zhang* et al. 2014).

2.1.8 Barotropic and baroclinic instabilities

Barotropic instabilites are generated when the speed of a current matches the speed of propagating barotropic waves - generating a situation where kinetic energy is transferred from the current to the wave. This can lead to a very large disturbance in the flow and make it break up. A barotropic instablity can take place in a current that is devoid of density gradients and is only a product of the speed and shape of the current and topography.

Baroclinic instabilities only take place in a baroclinic flow, flows in where density gradients are not parallel to pressure gradients. A baroclinic flow does not exclude barotropic instabilities, most instabilities in the ocean are mixed barotropic-baroclinic instabilities. In baroclinic instability, kinetic energy is drawn from the potential energy stored in the sloping density surfaces. The instabilities are generated by an interaction of vortices generated by the conservation of potential vorticity. When a water column is stretched, it will get a cyclonic relative vorticity and when squeezed an anticyclonic relative vorticity. Under certain conditions interaction of water columns that are stretched and squeezed leads to an unstable growth of vorticity, effectively transforming potential energy to kinetic.

2.1.9 Altimetry

Satellite altimetry is the measurement of surface topography using satellites. In oceanography, the measurement of sea surface topography is relevant. The satellite sends a pulse of microwave radiation towards the surface, part of the radiation is reflected back to the satellite, and the time it takes for the signal to return is used to calculate the sea surface height (SSH). Disruptions from the atmosphere is accounted for (*Chelton* et al. 2001).

When barotropic currents are approximately in geostrophic balance, they will be evident in the slope of the sea surface. This enables the calculation of geostrophic velocities from gradients in SSH using the equation of geostrophic velocity (Equation 2.4) and hydrostatic balance, $\frac{\partial p}{\partial z} = -\rho g$.

$$v_g = \frac{g}{f}\frac{\partial \eta}{\partial x}, \qquad u_g = -\frac{g}{f}\frac{\partial \eta}{\partial y} \tag{2.11}$$

where η is SSH.

2.1.10 The Okubo-Weiss Parameter

The Okubo-Weis Parameter (W) is the balance between stretching and shearing deformation against vorticity, (*Okubo* 1970; *Weiss* 1991):

$$W = (\frac{\partial u}{\partial x} - \frac{\partial v}{\partial y})^2 + (\frac{\partial v}{\partial x} + \frac{\partial u}{\partial y})^2 - (\frac{\partial v}{\partial x} - \frac{\partial u}{\partial y})^2 \tag{2.12}$$

The two terms with a positive sign represent stretching of the flow. The term with a negative sign is vorticity. In a 2-dimensional flow where vorticity dominates shear, $W < 0$, when stretching dominates $W > 0$. *Isern-Fontanet* et al. (2003) showed that it is possible to detect eddies from SSH observed with satellite altimetry using the Okubo-Weiss parameter. Areas of eddy motion will have a negative Okubo-Weiss parameter.

2.2 GEOGRAPHIC LOCATION AND OCEANOGRAPHIC CONTEXT OF THE LOFOTEN BASIN

In this section, I will outline the significant topographic and oceanographic features of the Nordic Seas in general, and of the Lofoten Basin (LB) in particular.

2.2.1 Topography of the Nordic Seas and the Lofoten Basin

The Nordic Seas are marginal seas located south of Svalbard and north of Iceland (see Figure 2.2). To the south, it is separated from the North Atlantic by the Greenland-Scotland ridge. The deepest sills at this border are the Faroe Bank Channel, that is ~850 m deep and located between Faroe and Shetland Islands, and the ~850 m deep Denmark Strait situated between Greenland and Iceland. North, the Nordic Seas border the Arctic Ocean. The primary connection to the Arctic Ocean is the ~2600 m deep Fram Strait, between Svalbard and Greenland. A mid-ocean ridge system that divides the Nordic Seas in two extends from the North Icelandic shelf to Jan

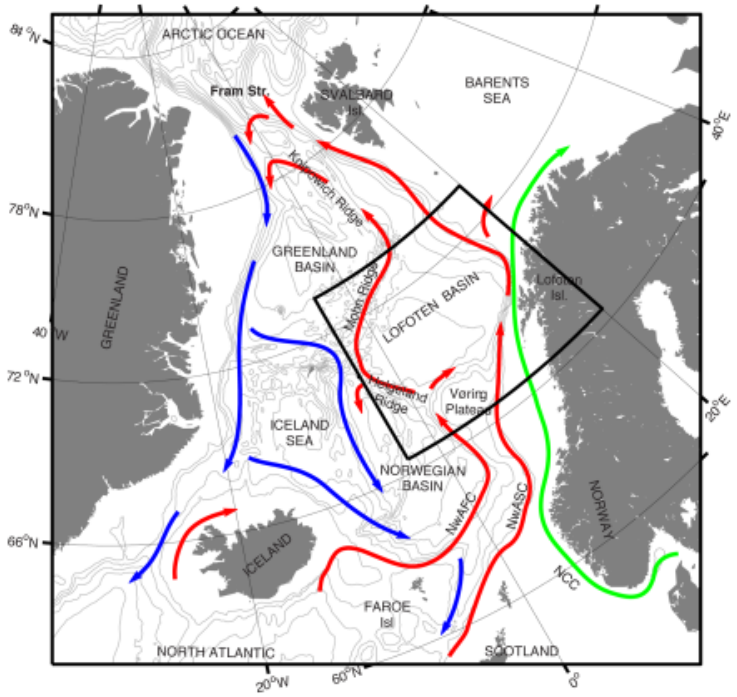

Figure 2.2 – Currents and bathymetry in the Nordic Seas. Red arrows indicate warm currents, and blue arrows cold deeper currents. Figure from *Raj* et al. (2016a)

Mayen (the Kolbeinsey Ridge) and continues from Jan Mayen along the Mohn Ridge to about 73.5° N. From here, the Knipovich Ridge continues to the Fram Strait. On the western side of the mid-ocean ridge is the Greenland Sea that contains two deep basins. Of these two the Greenland Basin is the largest and deepest with depths down to 3600 m. The smaller Borea Basin is to the north of the Greenland Basin. The Iceland Sea is located south of the Greenland Sea. The Iceland Plateau is the area east of the Kolbeinsey Ridge between Iceland and Jan Mayen. East of the plateau there is a small basin that is more than 2200 m deep. The easternmost of the Nordic Seas is called the Norwegian Sea. It has two deep basins, the Norwegian and the Lofoten Basin (LB). The Norwegian Basin is the largest and deepest basin in the Nordic Seas. It has depths down to ∼3600 m and extends northward from the Iceland-Faroe Ridge and eastward from the Iceland Plateau to the Vøring Plateau.

The LB is ∼3200 m deep. It is separated from the Norwegian Basin by the Helgeland Ridge to the south-west and the Vøring Plateau to the south. To the north-west, the Mohn Ridge divides it from the Greenland Sea. To the north and north-west, the basin is constricted by the continental slope. The continental slope has a moderate angle to the north-west where the LB borders the Barents Sea. To the east, it is steeper, especially along the Lofoten and Vesterålen Island (*Blindheim* et al. 2005).

2.2.2 The Norwegian Atlantic Current

The Norwegian Atlantic Current is an elongation of the North Atlantic Current that carries warm and saline waters originating from the Gulf og Mexico. This water flows into the Nordic

Seas at its southern border. In the Nordic Seas it continues the northward flow into the Arctic, where it sinks and flows back south again, playing an essential role in the Meridional Overturning Circulation.

The main inflow of warm and salty water into the Nordic Seas from the North Atlantic Current occurs in three locations: the Eastern Denmark Strait, the Iceland-Faroe Ridge and the Faroe-Shetland Channel. The inflow over the Faroe Ridge and the Faroe Shetland Channel is the primary source of Atlantic Water in the Nordic Seas, and form the Norwegian Atlantic Current (NwAC) (*Blindheim* et al. 2005).

The branch that goes over the Iceland Faroe Ridge has the form of a meandering frontal jet, going northeastward along the Iceland-Faroe Ridge into the Norwegian Sea where it turns northward after passing the Faroe Island and takes its part as the western branch of the NwAC, called the Norwegian Atlantic Front Current (NwAFC). The NwAFC then follows the topography on the west side of the Vøring Plateau. When it meets the LB, it splits into two parts. The main part of the NwAFC follows the Mohn Ridge on the east side of the basin, and follows the Knipovich Ridge toward Fram Strait (*Orvik* et al. 2002).

The branch that enters north of the Faroe-Shetland Channel continues along the continental slope with some small branches going into the North Sea. It goes northward following the Norwegian coast as the Norwegian Atlantic Slope Current (NwASC). North in the LB, it branches, with one branch going into the Barents Sea and the main part continues along the Norwegian shelf toward Fram Strait (*Orvik* et al. 2002).

Mork et al. (2010) reported the flow for the two branches of the NwAC at the Svinøy section, located at about 63.5°N. In the following the flow rate is given in Sverdrup (Sv), $1\,\mathrm{Sv}{=}1 \times 10^6\,\mathrm{m^3\,s^{-1}}$. The total flow of the NwAC was found to be $5.1 \pm 0.3\,\mathrm{Sv}$. The NwAFC contributing with $1.7 \pm 0.2\,\mathrm{Sv}$ and the NwASC $3.4 \pm 0.3\,\mathrm{Sv}$. Earlier studies have found higher estimates, *Orvik* et al. (2001) estimated 4.2 Sv for the NwASC and 3.4 Sv for the NwAFC. Adding up to a total of 7.6 Sv for the NwAC. They also described the NwAFC at the Svinøy section as a 30 - 50 km wide and approximately 400 m deep jet in the Arctic Front and the NwASC as a topographical trapped current 30 - 50 km wide.

The NwASC has a strong seasonal signal, with a maximum transport in Dec-Feb (above 7 Sv) and minimum (4 Sv) in Jun-Aug. The NwAFC has a smaller seasonal cycle (± 2 Sv) co-varying with the NwASC. In contrast the inter-annual variability is large in the NwAFC and small in the NwASC (*Mork* et al. 2010).

Rossby T. et al. (2009) showed that there is exchange between the NwAFC and NwASC current in the area around the Svinøy section. Several subsurface floats following the NwAFC current from the Iceland-Faroe ridge were transferred to the NwASC there.

Using hydrography data from May 2000, *Gascard* (2004) investigated the NwAC in the LB. They found that the NwAFC has a baroclinic volume transport of 2.4 Sv as it passes 72°N on the western border of the LB. They calculate the NwASC to have a total transport of 7.2 Sv, (4.9 Sv baroclinic and 2.3 Sv barotropic) just off the Lofoten Islands. The steep continental slope of Lofoten and Vesterålen is where the NwASC reaches it highest speed (*Poulain P.-M.*

et al. 1996).

2.2.3 Hydrography of the Lofoten Basin

Compared to the other basins in the Nordic Seas, the LB stands out as the largest pool of warm Atlantic Water (*Rossby* et al. 2009). The climatologic Atlantic Water layer in the LB reaches depths larger than 700 m (*Richards* et al. 2015).

The reason for the deep layer of Atlantic Water in the LB is believed to be mesoscale eddies formed by instabilities in the NwASC propagating into the basin and being trapped there by the topographic contours; an overview of literature is given below. As a result of the warm water input, there is a large winter surface heat flux out of the basin. The LB has a wintertime buoyancy loss of $-6.0 \pm 0.7 \times 10^{-8}\,\mathrm{m^2\,s^{-3}}$ (*Isachsen* et al. 2007). The Lofoten Basin is responsible for one third of buoyancy lost by the Nordic Seas in winter despite having only one fifth of the total area (*Richards* et al. 2015). Heat loss given by the SOC97 climatology in the Lofoten Basin is approx $60\,\mathrm{W\,m^{-2}}$ (*Isachsen* et al. 2007). With an estimated surface area of $400\,\mathrm{km} \times 400\,\mathrm{km}$, a total heat loss is 9.6 MW. An annual net heat loss of $80\,\mathrm{W\,m^{-2}}$ for the central parts of the basin is found by *Richards* et al. (2015).

The main gradients of temperature and salinity in the Nordic Seas are along the Jan Mayen, Mohn and Knipovich ridges (*Rossby* et al. 2009). The LB has cyclonic mid-depth, 1000 - 1500 m, circulation (*Voet G.* et al. 2010).

2.2.4 The Lofoten Basin Eddy

The Lofoten Basin Eddy (LBE) is a permanent anticyclone, which resides in the center of the deep western part of the LB. It has a cyclonic drift, in agreement with the mid-depth circulation of the basin (*Raj* et al. 2015). The LBE has a mean radius of $18 \pm 4\,\mathrm{km}$ and the Atlantic Water layer in the LBE exceeds 1000 m (*Yu* et al. 2017). The LBE is an important feature, often linked to the deep layer of Atlantic Water in the LB. It is believed that the LBE is maintained through merging with anticyclonic eddies that propagate from the NwASC (eg. *Volkov* et al. 2015; *Raj* et al. 2015; *Søiland* et al. 2016) and is stabilised by the bottom topography (*Köhl* 2007).

2.3 SHORT REVIEW OF PREVIOUS STUDIES ON EDDY ACTIVITY IN THE LOFOTEN BASIN

Several studies focus on the oceanography and eddy activity in the LB. Here I will gategorize these in 4 groups. Studies that confirm the LB as an area with a high eddy activity; those that investigate the breakaway of eddies from the NwASC current; others that look at the hydrographical properties of eddies in the LB in general; and finally studies that focus on the properties of the LBE in particular.

Observations of eddy activity in the Lofoten Basin

Several drifter-based studies have observed a high eddy activity in the LB. The first major campaign was in the period June 1991 to August 1994 (*Poulain P.-M.* et al. 1996) with 107 drifters drogued to 15 m released in the Nordic Seas. Eddy drifters from all major deployment sites ended up in the LB, motivating Poulain to coin the basin as "The maelstrom of the surface water masses". High eddy activity was observed in the LB, with Eddy kinetic energy (EKE) surpassing $400\,\mathrm{cm^2\,s^{-2}}$. An area north of Vesterålen in the eastern part of the basin had the highest measured value of EKE (EKE $> 600\,\mathrm{cm^2\,s^{-2}}$). *Poulain P.-M.* et al. (1996) also noted that most of the observed long-lived mesoscale features occurred in the LB and that the principal axes of variance showed a larger variance in the east-west then the north-south direction in the LB, this was explained as a "jet-like structures" going westward from the NwASC. A similar pattern of EKE was found in *Jakobsen Philip K.* et al. (2003) from drifters buoyed at 15 m also deployed in the Nordic Sea. *Jakobsen Philip K.* et al. (2003) calculated the eddy flux ,$v'u'$, that indicated a net eddy transport from the NwASC into the LB. *Volkov* et al. (2013) analyzed 17 years (1995-2011) of satellite observed altimeter data. The velocity of eddy propagation in the basin is calculated with a space-time lagged correlation analysis of SSH, showing that the eddies propagate in a cyclonic circulation around the center of the basin. With an average propagation velocity of 2 - 2.5 $\mathrm{km\,d^{-1}}$ at the Vøring Plateau escarpment to nearly 4 $\mathrm{km\,d^{-1}}$ along the cyclonic spiral of eddy propagation in the LB. This circulation pattern resembles the mid-depth circulation found in *Voet G.* et al. (2010), indicating that eddy propagation in the LB is affected by deep currents rather than surface currents. Another study using altimetric data by *Chafik L.* et al. (2015), shows that the EKE energy in the LB is dominated by mesoscale activity. With a composite analysis of open available hydrographic data, they also track temperature anomalies propagating along the NwASC. They find a connection between positive temperature anomalies in the NwASC at the Svinøy branch and positive temperature anomalies entering the LB. The anomalies are visible in the eastern part in the basin 2 months after being detected at the Svinøy branch and have moved to the deepest part of the basin after 12 months. The temperature anomaly moves in compliance with the speed range of barotropic Rossby waves calculated in *Volkov* et al. (2013). This finding supports the view that there is a transport of Atlantic Water by mesoscale eddies and wave features from the NwASC into the LB. EKE was calculated to be up to $350\,\mathrm{cm^2\,s^{-2}}$ in the LB by *Rossby T.* et al. (2009).

Koszalka et al. (2011) used a drifter clustering technique instead of geographical bin averaging to analyze data from 360 drifters deployed in the Nordic Seas. The technique clusters drifters that are geographically close together using an algorithm, allowing a higher resolution than with bin averaging. Like previous studies, they find a high level of eddy kinetic energy (up to $500\,\mathrm{cm^2\,s^{-2}}$) of the NwASC in the LB. Due to the strict topographic steering in the Nordic Seas - the mean current mostly follows the topographic isobath line, they calculate the cross isobath eddy diffusivity, finding the highest levels of the continental slope in the interior of the LB. The diffusivity is low in the NwASC where the eddies are generated but higher offshore, indicating that mixing due to mesoscale eddy activity take place offshore.

Raj et al. (2016a) used a satellite altimetry derived dataset of mesoscale eddies in the LB for the period 1995-2013 (an extension of the dataset is used in the thesis, for a detailed description of the algorithm see section 2). The study confirms that the basin is an area with rich eddy activity and finds the regions with the highest eddy activity to be the deepest western part of the basin and near the slope in the eastern part of the basin. It also finds that anticyclone has a longer lifetime then cyclones in the basin. The areas with the longest-lived eddies are in the central part in the area around the LBE and the western part outside the slope current. The lifetime of an eddy is strongly correlated to the eddy intensity. In *Raj* et al. (2016b), a cyclonic eddy drift pattern in the LB is found.

Eddies breaking from the NwASC

A breakaway of water masses from the NwASC as it passes west of Lofoten was observed by *Rossby T.* et al. (2009). In the study, 22 acoustically tracked RAFOS floats were deployed south of the Iceland-Faroe ridge and set to be neutrally buoyant at a nominal depth of 200 m in the deployment region. 12 of the floats followed the NwASC northward and reached the LB where half of them broke away from the slope, identifying a major breakaway of water masses - they note that the breakaway can be seen in a deepening of the climatological pycnocline just of the Lofoten Islands. The breakaway of subsurface drifters was much more pronounced than for surface drifters - compared with *Poulain P.-M.* et al. (1996). *Isachsen* et al. (2012) used openly available data from over 400 drifters that span the period 1990-2010, satellite altimetry, and ROMS numerical ocean model to investigate eddy heat fluxes in the Nordic Sea. Their findings showed that the eddies in the Nordic Seas cool water warmer then 6°C and warm colder water, and that the greatest cooling of the NwAC takes place as it passes the Lofoten Basin. The study affirms that there is a systematic tendency for the eddies to transport heat from the NwAC into the Norwegian and Lofoten basin. *Isachsen* (2015) studied instabilities in the NwASC, Showing that the fastest unstable growth takes place over the steepest part of the continental slope outside the Lofoten-Vesterålen Islands and that the generated EKE is advected away from the generation regions by nonlinear processes. In *Rossby* et al. (2009), they make a simple calculation based on an observed AC that it takes 24 eddies with a radius of 40 km and depth of 300 m propagating from the slope and into the basin to balance the 60 $W\,m^{-2}$ heat loss found in *Isachsen* et al. (2007). This would require a mass transport of 1.2 Sv.

Hydrographical observations of Lofoten Eddies

In *Rossby* et al. (2009) hydrographic measurements of an anticyclone observed by chance at in the LB at 9°E and 69°N is presented, and they state that similar features are common in the LB.

One of the few studies that used hydrographic in situ measurements to describe eddies in the LB is that by *Richards* et al. (2015). They investigated anticyclonic eddies in the LB using data from a mooring deployed at (69.655° N, 6.962° E). In the period May 2011 to September 2012, they observed 22 positive temperature and salt anomalies classified as possible anticyclonic eddies. Among these, 6 fitted the assumption of a Rankine vortex velocity field allowing eddy

variables to be extracted. Over the top 500 m, these eddies had a mean radius of 17 km. Mean propagation speed of 6 cm s^{-1} and a mean maximum rotational speed of 22 cm s^{-1}. Mean isopycnal potential temperature, and salinity anomalies relative to the background was 0.14 °C and 0.01. Three of the eddies were propagating to the south-southwest and the other half propagated toward the north-northeast - the direction that fits with the mean eddy trajectories found in *Volkov* et al. (2013). Two of the six identified eddies were described in detail. The first eddy passed the mooring in April, had a radius of 32 km and was found to be of mode water. The salt and temperature anomaly was very weak or not present in the top 400 m, suggesting that most of the original heat content was lost during its lifetime in the LB. The second eddy was observed in August and had a radius of 12 km, a clear temperature and salinity anomaly from the surface and down to 1200 m, and hydrographic properties consistent with the slope current properties. Both eddies propagated northward. The mode water eddy suggests that eddies can have a long lifetime, similar to the cooling period in the basin, and can be an important location for convection and water mass transformation.

A coincidental temperature transect of a Lofoten Eddy is presented in *Rossby* et al. (2009), and they note that similar features are common in hydrographical data from the LB. Another example of an accidental observation of an anticyclone in the Lofoten basin is presented in *Søiland* et al. (2016) were an anticyclone close to the usual position of LBE was observed. The eddy was found to have a radial scale of about 27 km, heat content of 10 EJ, Dynamic amplitude of 0.16 m, Total eddy potential energy of 1.1 PJ, kinetic energy of 0.1 PJ, a very rough estimate of the frequency of -0.9f and a temperature anomaly of 0.8 °C. The velocity maximum of the eddy was found to be in the upper 300 m at 0.4 m s^{-1}. This study concludes that mesoscale eddies are responsible for the deep layer of Atlantic Water in the LB and that only a small fraction of the anticyclones in the basin can be merged with the LBE, considering how much energy and water they contain.

The Lofoten Basin Eddy

Several studies focus on the superstar of the LB, the permanent LBE. *Köhl* (2007) used an ocean models to investigate the LBE. The results suggested that the LBE is driven by eddies that are created by instabilities in the slope current and propagate to the center of the Basin. The model runs show that the topographic conditions attract anticyclones to the center of the basin and that the topography has a stabilizing effect on anticyclones; in line with *Benilov* (2005). They also use altimetry SSH data to show a general westward eddy drift, especially for anticyclones.

Raj et al. (2015) used altimetric data to show that the LBE is fed with energy through eddy merging and that it resides in the deepest part of the basin. Using current and hydrographic measurements from ship *Søiland* et al. (2016) investigated the LBE over several years. They concluded that it is plausible that the LBE is a permanent feature of the LB. In *Yu* et al. 2017, glider and altimetry data have been used to investigate the LBE. They found that the LBE has a mean radius of 18 ± 4 km and a maximum velocity of 0.5 - 0.7 m s^{-1} located between 700 - 900 m. They also found that the altimeter-derived variables, which are calculated with the same

method as in *Raj* et al. (2015), *Raj* et al. (2016b), and *Raj* et al. (2016a), overestimate the radius of the LBE by a factor of 2, but accurately describe the location. *Fer* et al. (2018), used measurements from a cruise in June 2016 to investigate the stratification, currents and turbulent dissipation of the LBE. The LBE is found to have a velocity maximum of $0.8\,\mathrm{m\,s^{-1}}$ located at 925 m depth 22 km from the center, and enhanced turbulence at the base in the core and the rim.

3 | Methods and Data

3.1 DATA

An overview of the data used is presented in this section. The data set consists of a satellite-derived eddy product and observations from 8 glider deployments. The eddy product is derived from altimetry data using a combination of sea surface height and the Okubo-Weiss parameter. The glider data are collected using Seagliders deployed in the Lofoten Basin from 2012 to 2017.

3.1.1 Satellite derived eddy product

The eddy dataset is the same used in *Raj* et al. (2015), *Raj* et al. (2016a), and *Raj* et al. (2016b) with a temporal extension. The dataset covers the period from Jan 1, 1993 to May 15, 2017 and has a spatial extent from 6.8°W to 20.0°E and 65.9° to 74.4°N. It contains a total of 25118 realizations of eddies. Every eddy has an unique identification number and daily values for eddy intensity, vorticity, radius, amplitude, propagation speed and the position of eddy center given in latitude and longitude.

As input, the sea level anomaly (SLA) from the global ocean gridded l4 sea surface heights product produced and distributed by Copernicus (http://www.marine.copernicus.eu/) is used. Copernicus use the SL-tac multi-mission altimeter data processing system that uses all available satellite altimetry data. The product has a global coverage and a 0.25° x 0.25° spatial resolution on a Cartesian grid and a daily temporal resolution ("Access to products" 2018). The grid size at 70° N is then 9.5 x 27.8 km.

The eddy tracking procedure uses a combination of SSH and the Okubo-Weiss parameter to classify eddies. Using a combination of W and closed isolines in SLA leads to better results than using the one without the other.

The procedure follows the method used in *Halo* (2012) and *Halo* et al. (2014). The procedure can roughly be divided into four parts and is described below.

- The first step in the detection scheme is to calculate the geostrophic velocity anomalies from the SLA using the geostrophic relations:

$$u' = \frac{-g}{f}\frac{\partial h}{\partial y} \tag{3.1}$$

$$v' = \frac{-g}{f}\frac{\partial h}{\partial x} \tag{3.2}$$

g is the gravitational acceleration, h is SLA and x and y are the zonal/meridional coordinates,u' and v' are the zonal and meridonal geostrophic velocity anomalies.

- The second step step is to calculate the Okubo-Weiss parameter,W, using the geostrophic velocity anomalies (Equation 2.12). Two passes of a Hanning Smoother is applied to W in order to reduce the grid scale noise. Then regions with $W < 0$ (regions that are dominated by vorticity) are selected.

- The third step is to find regions located within closed SLA isolines. The height interval between isolines are set to $\Delta h = 2\,\text{cm}$ and a limit of maximum 500 km is set on the equivalent of a diameter (the diameter of a circle with an area corresponding to the surface area of the selected region).

- The fourth step is to combine regions within closed SLA isolines with regions that have negative W. If a region is both within a closed isoline and has a negative W, it is classified as an eddy.

The radius, r, of the eddies is calculated from the surface area of the respective eddy:

$$r = \sqrt{\frac{A}{\pi}}. \tag{3.3}$$

The Eddy Kinetic Energy (EKE) is computed from the geostrophic anomalies with the equation:

$$EKE = \frac{u'^2 + v'^2}{2}. \tag{3.4}$$

The eddy intesity (EI) is defined as the area-weighted mean EKE over the eddy area, A:

$$EI = \frac{1}{A}\int_A (EKE)dA. \tag{3.5}$$

The procedure is carried out on every time step of the SLA data. Then an eddy tracking algorithm, following *Penven* et al. (2005), is used to find the trajectories of the eddies. e1 is the eddies in the first time step, e2 is in the second. A non dimensional distance, $X_{e1,e1}$, is defined as:

$$X_{e1,e1} = \sqrt{\frac{\Delta X^2}{X_0} + \frac{\Delta R^2}{R_0} + \frac{\Delta \omega R^2}{\omega_0}}, \tag{3.6}$$

were ΔX is the spatial distance between eddy centres of e1 and e2, ΔR is the difference in diameter, $\Delta\omega$ is the difference in vorticity. X_0 is a characteristic length scale in the LB set to 25 km, ω_0 a characteristic vorticity set to $10^{-5}s^{-1}$, R_0 a characteristic radius set to 25 km. The pair of eddies in e2 and e1 that minimizes $X_{e1,e1}$ is set to be the same eddy. The eddies also have to preserve their rotational direction (polarity). Every detected eddy is given an unique identification number. There is no limit to the lifetime of the observed eddies.

Table 3.1 – Details of the glider deployments

Mission	Deployed	Recovered	Duration(days)	Glider number	Dives	Dives < 500 m
M1	4. Jul 2012	25. Jan 2013	205	SG559	617	38
M2	14. Feb 2013	16. Sep 2013	214	SG562	680	5
M3	11. Oct 2013	17. Feb 2014	129	SG561	457	51
M4	26. Feb 2014	1. Nov 2014	248	SG563	831	4
M5	18. Dec 2014	18. Jul 2015	91	SG562	91[a]	3
M6	18. Dec 2014	18. Jul 2015	212	SG559	699	9
M7	4. May 2016	13. Jan 2017	253	SG561	818	14
M8[b]	13.Jan 2017	24. July 2017	191	SG563	649	10

[a]Mission lasted 212 days, sampling near the Mohn Ridge not included
[b]Due to a technical issue temperature and salinity is not recorded for the last 17 days of the mission

3.1.2 Seaglider data

Seagliders are autonomous underwater observation platforms which glide through the ocean by adjusting their buoyancy. Seagliders can be equipped with a multitude of observational sensors (temperature, conductivity, oxygen, fluorescence, turbidity). As a means of steering, they use buoyancy, wings to glide and the position of the battery pack to alter their pitch and roll. When beginning a descent, a Seaglider becomes negatively buoyant. As it sinks, the wings give it forward propulsion while it navigates with dead reckoning in a given compass direction. When the Seaglider reaches the preset diving depth, it expands an internal oil bladder making it positively buoyant, adjusts the position of the battery, and glides upwards toward the surface. At the surface, it transmits the collected data and the current position to the operator with Iridium, receives a new direction and makes another dive, making a sawtooth trajectory through the ocean. The gliders used here dive to 1000 m depth max. Using the discrepancy between the given direction of the dive and the position of the glider when it surfaces, a depth-integrated current can be calculated. Seagliders can collect data both on the downcast and the upcast (*Eriksen* et al. 2009).

The first glider was deployed in July 2012 and the last in May 2017. The first six deployments, M1-6 (*Fer* et al. 2017), have been steered by the Norwegian Atlantic Current Observatory (NACO), as part of an observational infrastructure to observe variability in the North Atlantic Current. The last two deployments, M7-8, have been facilitated by the PROVOLO project. Details of the deployments are shown in Table 3.1.

All eight missions transect the LB. Many of the missions spend a large amount of time inside the LBE, the only mission that evades the LBE completely is M1. In *Yu* et al. 2017 M1-6 was used to study the LBE in detail. Figure 3.1 shows the trajectory of the gliders.

The glider raw data were processed using the University of East Anglia Seaglider tool-

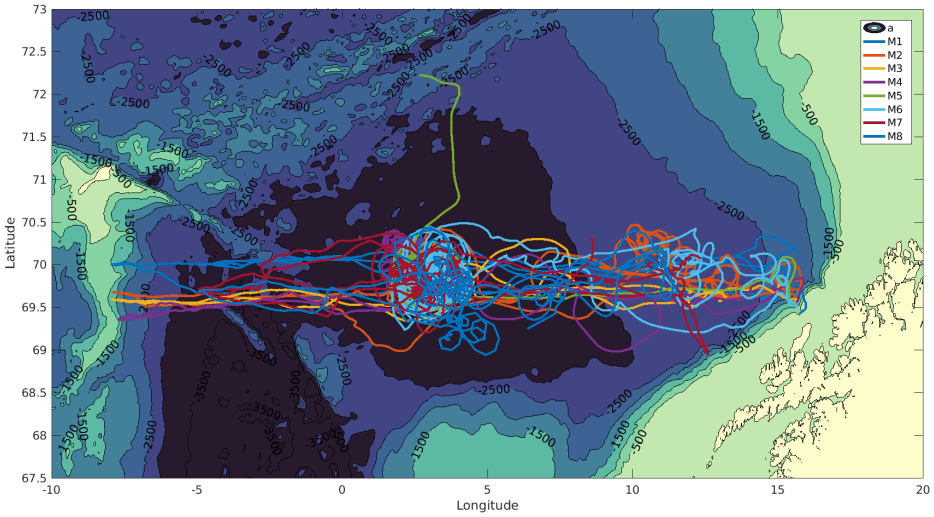

Figure 3.1 – Trajectory of all glider deployments.

box (http://bitbucket.org/bastienqueste/uea-seaglider-toolbox). Hard maximum and minimum threshold values were applied to exclude and interpolate outliers. The Conservative Temperature and Absolute Salinity measurements were compared to accurate hydrographic data from ships. Absolute Salinity was corrected by a small constant offset obtained by a least-squares fitting of the glider data between 700 m and 1000 m to reference linear T/S relationship corresponding to the mixing line between the Atlantic Water and the deep waters below 700 m (*Fer* et al. 2017).

The Seagliders presented here collected data during both dive and climb, the data is interpolated to 1-decibar vertical intervals, latitude and longitude position is interpolated on a line between the surfacing position. One dive-climb pair gives two sloping profiles of the upper ocean that can be treated as a vertical profile since the slope of the glider trajectory is much steeper than the slope of the ocean isolines (*Testor* et al. 2010). A depth integrated current velocity is obtained at the location in the middle of consecutive surfacings.

Sampling rate of M1-6 is typically every 14 - 32 s, glider vertical speed typically 7 - 10 $cm\,s^{-1}$. This gives a vertical resolution of 1 - 3 m. M7 has a sampling rate of 10 s and a vertical speed of around 10 $cm\,s^{-1}$ giving a vertical resolution of 1 m. M8 has a sampling rate of 18 - 20 s and a vertical speed of around 8 $cm\,s^{-1}$ giving a resolution of about 1.4 - 1.6 m.

3.1.3 Gimsøy section

I also use a data set from the Gimsøy section that extends north-westward from the continental shelf outside the Lofoten Islands into the LB, location of the section can be seen in Figure 4.1. The data set contains 993 hydrographic profiles taken from ship in the period 2000 - 2016. It is a repeated standard section performed by the Institute of Marine Research.

3.2 METHOD

3.2.1 Characterising eddies

In this section, I will describe the procedure and methods used for characterizing eddies in the LB using glider data.

Locating eddies in the data

The first step toward characterizing the eddies captured by the gliders is a visual inspection of the data. To enable this, I developed a tool that shows how the gliders are moving relative to the satellite-detected eddies. A picture, like the one in Figure 3.2, is generated for each day of glider sampling. The pictures show the trajectory, depth-averaged velocity, temperature and salinity from the gliders together with the position and radius of the satellite-detected eddies. For each day, the tail of the trajectory is 2 days. The trajectory of the glider and the observed velocities for the last two days relative to the satellite-derived eddy locations, can easily be visualized by browsing forward. By inspecting these pictures, eddies can be identified with a combination of the depth-averaged current structure and the decrease or increase in thickness of the warm water layer. An anticyclone will have a negative vorticity structure coinciding with a deep layer of warm water. A cyclone will have positive vorticity and a shallower layer of warm water. When a possible eddy is found, the profile index is noted and an appropriate time period is chosen to be analyzed further.

Detecting the position of an eddy center

In an idealized eddy, the velocity at all points will be perpendicular to a line drawn from the center. To define the position of an eddy center, I use an algorithm that finds the point most perpendicular to a subset of depth-averaged velocities, following the method used in *Bosse* et al. (2016). This method defines the eddy centers solely based on the depth-averaged current by minimizing a cost function:

$$g(x,y) = \frac{1}{n}\sum_{i=1}^{n}\left(v_i \cdot \frac{r_i(x,y)}{|r_i(x,y)|}\right)^2 \tag{3.7}$$

Where v_i is the depth averaged current for a dive at the position (x_i, y_i), r_i is the vector from (x, y) to (x_i, y_i), n is the number of dives included and is set to $n = 4$. The algorithm goes through the depth averaged velocities with an increment of two dives giving the center location as a function of time. Figure 3.3 shows an example for a detected center.

Since the ocean is rich in structure, the results have to be inspected manually and quality controlled. The points that look suspicious are rejected. The time attributed to an eddy center is defined as the mean time of the dives that constitute the set of velocities that defines the position. A two dive increment will roughly give a 12 h interval between detected centers.

In the cases where no good centers are found with $N = 4$ and an increment of two dives, the values are tweaked to find a combination that accurately describes the location of the eddy.

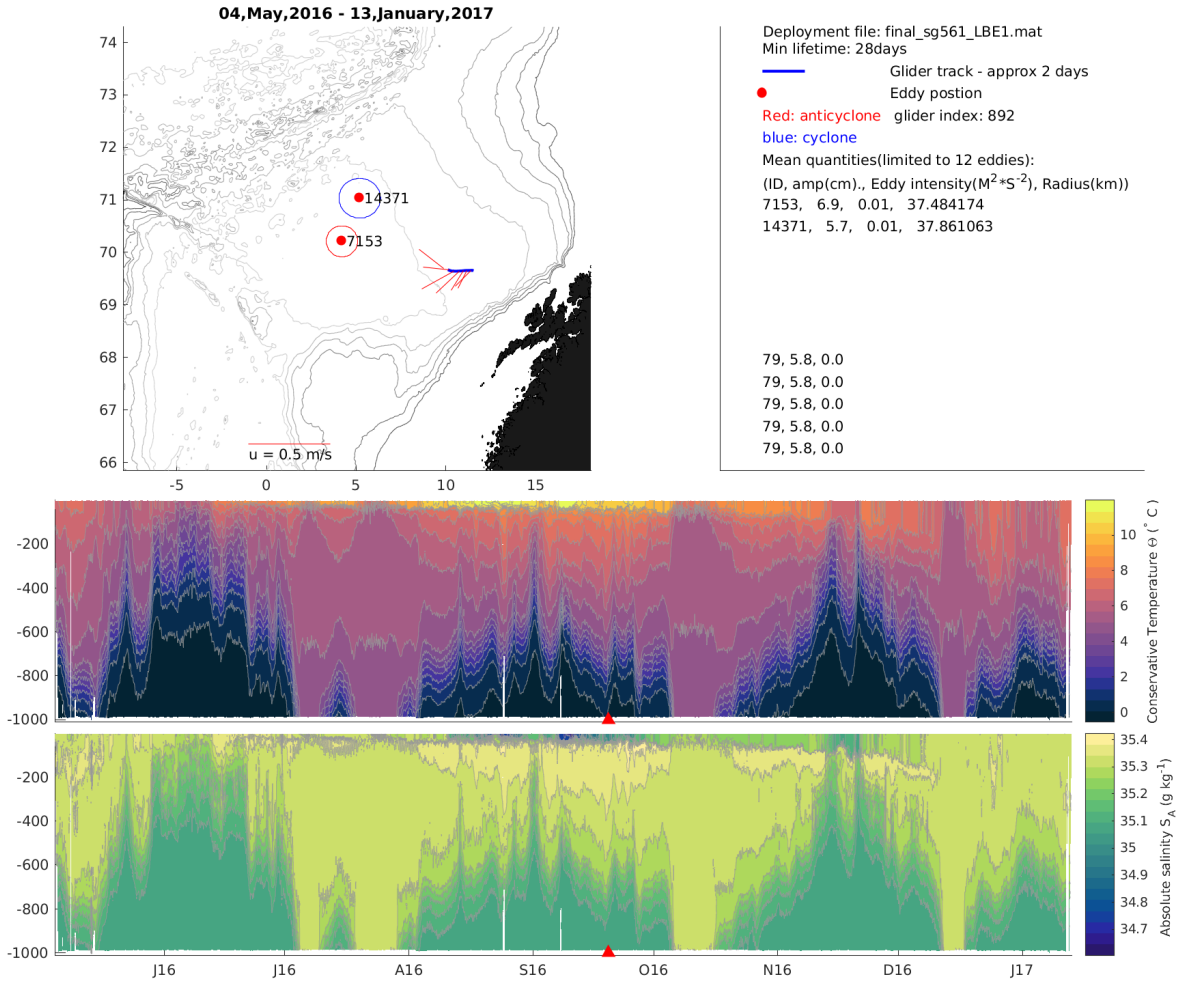

Figure 3.2 – Example of pictures combining glider and satellite derived eddy product generated for every day with glider samplings from the LB. The map shows position of eddies with a red marker and radius with a circle that is blue for cyclones and red for anticyclones. The glider trajectory for 2 days are shown with a blue line and arrows that show the depth-averaged velocity for the same time period. A red pointer in the temperature and salinity contour shows the current position on the timeline.

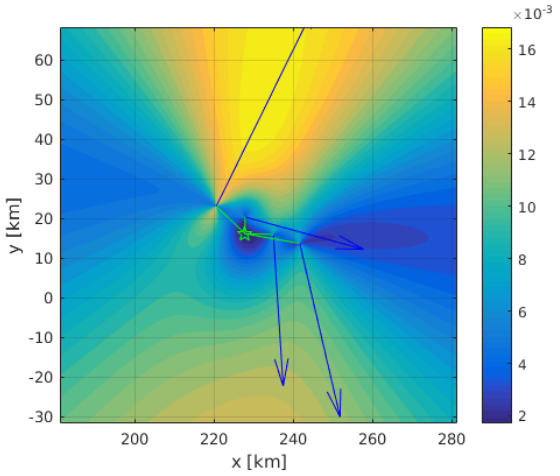

Figure 3.3 – Example of the minimized cost function. The colorbar show the size of $(g(x, y)$ and the green star is placed on the position with the minimum value defined as the eddy center.

Before finding the eddy centers the position of the glider data is transformed to a flat earth projection with $lat = 70°$N, and $lon = 5°$E, as the reference position.

Interpolating and smoothing eddy trajectory

The points that are kept after the manual assessment of the eddy centers are transformed back to geographical coordinates. If there is more than one point that passed the quality control, a trajectory with 1 h intervals between centers is linearly interpolated. Then the interpolated trajectory is smoothed with a moving average using a 36 h boxcar window.

To connect every profile and dive-averaged quantity to an eddy center, the smoothed trajectory is linearly interpolated to the time of every measurement. Measurements approximately within four times the eddy radius is included in the analysis of the eddy, depending on the presence of other eddies or fronts in the surrounding. The measurements outside the time period of the eddy center trajectory are attributed to the center closest in time.

Binning of temperature and salinity

In the following procedures, an eddy is assumed to be symmetric, circular and "frozen" during the sampling period. Since we are assuming that the eddies are symmetric, measurements are reorganized in term of absolute distance from the attributed center. Then the mean salinity, temperature and density profiles are calculated in 3 km horizontal and 5 m vertical bins.

Before smoothing, the section is reflected along the x-axis, to respect the eddy symmetry. Then, it is smoothed horizontally with a 9 km box car window and vertically with a 15 m box car window. If a bin does not contain any profiles the smoothing will assign the bin a value that is a mean of the surrounding bins. The smoothing reduces noise from high frequency variability, like internal waves.

Fitting azimuthal depth-averaged velocity to theoretical velocity structure

To isolate the motion that is connected to the eddy, the depth-averaged velocity is partitioned in two components: azimuthal and radial relative to the eddy center. We assume that only the azimuthal velocity is connected to the eddy velocity field. The absolute value of the azimuthal velocity is binned in the same manner as for temperature and salinity, but is not smoothed.

Since the current observations are affected by the background currents and not decay out to zero, we choose to fit a theoretical velocity field to portray the inherent characteristics of the eddy. To find this, the binned azimuthal velocity is least-squares fitted to two different velocity models. The Rankine vortex (eq 3.8) is in solid body rotation from the center to the velocity maximum, V_{max}, then decays as $\frac{1}{r}$ outwards.

$$v_\theta = \begin{cases} V_{max}\frac{r}{R}, & \text{for } r < r. \\ V_{max}\frac{R}{r}, & \text{for } r > R. \end{cases} \tag{3.8}$$

An alternative velocity field is the Rayleigh vortex corresponding to a Gaussian geopotential anomaly:

$$v_\theta = V_{max}\frac{r}{R}e^{\left(-\frac{r\sqrt{2}}{R}\right)^2}\frac{1}{e^{-0.5}} \tag{3.9}$$

The two velocity structures are fitted to the absolute azimuthal velocities. With variables V_{max} and radial position of the maximum velocity, R. The value of the V_{max} in the least square fit range from 0.5 to 1.5 times the maximum of the binned absolute azimuthal velocities. R varies from 5 to 70 km. The combination of V_{max} and R that gives the least error is found for both velocity structures, and the theoretical vortex that gives the least error is defined as the depth averaged vortex velocity (v_{davv}) used in the further analysis. The eddy radius (R) is defined as the optimal radial position of V_{max}.

Absolute velocity

When the depth-averaged velocities for the upper 1000 m in the eddy are clearly defined, the next step is to find how these velocities vary in depth using the geostrophic shear induced by horizontal gradients in the density field. The dynamic height anomaly (Ψ) for the eddy field is calculated using the Gibbs sea water package (*McDougall* et al. 2011), and the depth-integrated geostrophic shear (v_{gs}) is obtained for every bin by dividing the horizontal gradient of Ψ with the local Coriolis parameter, f:

$$v_{gs} = \frac{1}{f}\frac{\partial\Psi}{\partial r}. \tag{3.10}$$

The absolute velocity (v_a) of the eddy field is found by subtracting the vertical mean of the vertically-integrated shear velocity from the vertically-integrated shear and add it to the depth-averaged vortex velocity (v_{davv}):

$$v_a(r,z) = v_{davv}(r) + v_{gs}(r,z) - \frac{1}{H}\int_{-1000}^{0} v_{gs}(r,z)dz. \tag{3.11}$$

This gives the absolute velocity for the eddy down to 1000 m under the assumption of geostrophic balance.

The maximum velocity in the v_a field is defined as v_{max}.

Eddy depth

The depth of an eddy is defined using a threshold on the vertical shear of absolute velocity. When $\frac{\partial v_a}{\partial z} > -10 \times 10^{-4}\,\mathrm{s}^{-1}$ and $v_a > \frac{1}{2}v_{max}$ at $r = R$ the bottom of the eddy is reached, this depth is defined as the eddy depth, D. The velocity limit is to make sure that the base is not defined to be in a low stratified core around v_{max} or at the surface of the eddy, where the shear can be negative.

Non-dimensional numbers

Three non-dimensional numbers are calculated for the eddies. The Rossby number (Ro), Burger number (Bu) and the Richardson number (Ri).

The Rossby number tells how well the assumption of geostrophy holds for an eddy. It is obtained from:

$$\mathrm{Ro} = \frac{2v_{max}}{Rf}, \tag{3.12}$$

which is the velocity difference across the eddy ($2v_{max}$) divided by the radius (R) and the local Coriolis parameter (f).

The Burger number is an indication of the importance of stratification and is calculated as:

$$\mathrm{Bu} = (\frac{N_{out}D}{fR})^2, \tag{3.13}$$

where N_{out} is an estimate of the mean buoyancy frequency of the water mass surrounding the eddy. It is defined as the mean of N from the surface to D and within the interval used for the reference profiles (defined below). R is the eddy radius, and D is the eddy depth. frequency.

To quantify the importance of shear within the eddy, the Richardson Number is calculated for every bin in the eddy field using:

$$\mathrm{Ri} = \frac{N^2}{\frac{\partial v}{\partial z}^2}, \tag{3.14}$$

Which gives an estimate of the balance between the stability of the water column vs the vertical shear. A low Ri near unity implies shear can be important, leading to shear instability of the flow, and turbulence and mixing. While the formal threshold for Kelvin-Helmholtz billows is $\mathrm{Ri} = \frac{1}{4}$, because of smoothing and coarse resolution $\mathrm{Ri} \approx O(1)$ is indicative of mixing.

Reference profiles

To estimate the properties of the water mass surrounding the eddy, reference profiles for salinity (S_{ref}), temperature (T_{ref}) and potential density (σ_{ref}) are calculated. The reference profiles are obtained by averaging the profiles from $3R$ to $4R$. When a signal from another eddy or a

clear anomaly in temperature and salinity is located within $[3R, 4R]$, another expedient interval is chosen.

Isopycnal and isobaric anomalies

Both isopycnal and isobaric anomalies are calculated. The isobaric anomaly is found by removing the relevant reference profile from the eddy fields of temperature, salinity and potential density giving the temperature anomaly field, t_a and salinity anomaly field, s_a.

Isopycnal temperature anomalies are found by removing the reference temperature obtained by linearly interpolating the reference temperature profile as a function of density to the reference density profile, $T_{ref}(\sigma_{ref})$. Isopycnal salinity anomaly is found in the same manner.

Isobaric salinity and heat content

The total content of heat relative to the background is found by integrating the heat content from the center of the eddy and out to the beginning of the interval used to calculate the reference profiles, and from the bottom of the eddy to the surface:

$$HC = \int_{-D}^{0} dz \int_{0}^{3R} 2\pi r dr \left[\rho_0 C_p t_a(r,z)\right], \tag{3.15}$$

where C_p is the heat capacity of seawater calculated with Gibbs sea water package using the local temperature and salinity of the bins, $\rho_0 = 1028\,\mathrm{kg\,m^{-3}}$ - a reference density value and t_a is the temperature anomaly of the bins. in practice: For every bin, $2\pi r dz C_p \rho_{ref} t_a$ is calculated, $dz = 5\,\mathrm{m}$ - the height of the vertical bins, and r is the radial distance from the eddy center. To find the total isobaric heat content of the eddy this is summed up vertically, from the surface down to , and trapezoidal integrated from $r = 0$ to $r = 4R$.

For the isobaric salinity content the same approach is followed, but the integration is done with the absolute salinity anomaly.

$$SC = \int_{-D}^{0} dz \int_{0}^{3R} 2\pi r dr \left[\rho_0 s_a(r,z)\right]. \tag{3.16}$$

Available Potential Energy and Eddy Einetic Energy

To enable the calculation of Available Potential Energy (APE), the isopycnal height anomaly Δz is calculated by interpolating columns of density to the vertical bin z coordinates as a function of σ_{ref} and withdrawing the vertical bin z coordinate. This gives the height anomaly of isopycnals, Δz, relative to the reference profile.

(APE) content of every bin is calculated using an equation for APE defined in *Hebert* (1988):

$$APE = \int_{-D}^{0} dz \int_{0}^{R_{di}} 2\pi r dr \left[\rho_0 N^2(r,z) \Delta z(r,z)^2\right] \tag{3.17}$$

The radial integration limit, R_{di}, is the dynamic integration limit of the eddy. It is defined as the radius when the addition of a new horizontal bin to the above integration makes the total amount of APE grow with less then 5%.

The Eddy kinetic energy (EKE) is calculated from:

$$EKE = \int_{-D}^{0} dz \int_{0}^{R_{di}} 2\pi r dr \left[\rho_0 \frac{v_a(r,z)^2}{2} \right] \tag{3.18}$$

The reason for implementing the dynamical limit for the EKE is that due to the ever increasing diameter of the eddy, the EKE does not converge.

Adjusting for cyclones

The procedure above is used as it stands for anticyclones. For a cyclone the velocity in the eddy will change signs, so the velocity found in the theoretical fit changes direction. As a consequence of this the eddy depth is defined as the point where the vertical shear is below $10 \times 10^{-4}\,\mathrm{s}^{-1}$ instead of above $-10 \times 10^{4}\,\mathrm{s}^{-1}$ as it is for an anticyclone, the sign of the vertical shear will be positive going downwards as the velocity decrease.

4 Results

4.1 MEAN STATE OF THE LOFOTEN BASIN

A mean of all the glider transects (excluding the profiles where a glider dwells in eddies for an extended period) reveals the large-scale zonal temperature and salinity structure of the upper 1000 m of the water column along the mean trajectory (Figure 4.1) of the glider. The mean of all the CTD-profiles taken along the Gimsøy section that stretches from outside Lofoten on the continental shelf and north-westward up to 70.5°N (Figure 4.1), shows some of the north-south structure of the basin and also crosses the NwASC that flows along the continental slope. The two transects meet at approximately 70°N and 9°E. The mean structure and the variability along the sections are presented here. The variability is quantified as the standard deviation over multiple realizations of the sections.

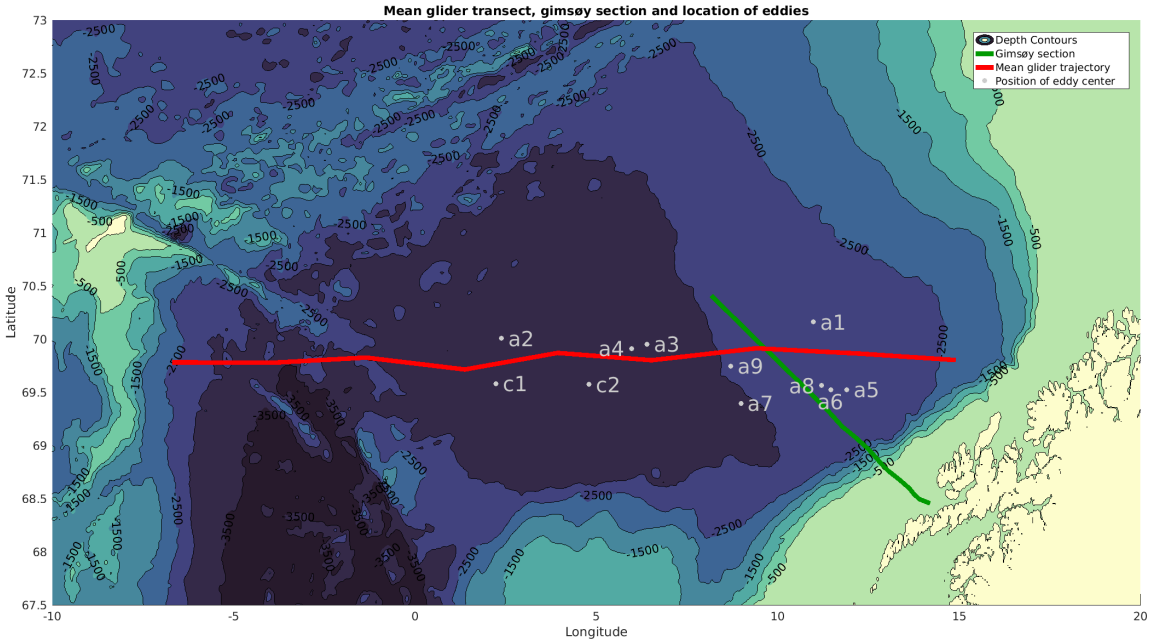

Figure 4.1 – The red line shows the trajectory of the mean basin transect, green line the Gimsøy section, and grey points and numbers the position of analysed eddies. A refers to anticyclones, and the numbers are the same as in Table 4.1. C refers to cyclones, and numbers are the same as in Table 4.2.

The zonal structure of the basin (Figure 4.2) shows that the warmest and fresh, and as a

consequence least dense, water of the LB is at the surface near the continental slope on the eastern edge of the basin. Further north, the surface temperature slowly drops while the salinity increases until the western front, at around 4°W, where the surface temperature drops quickly.

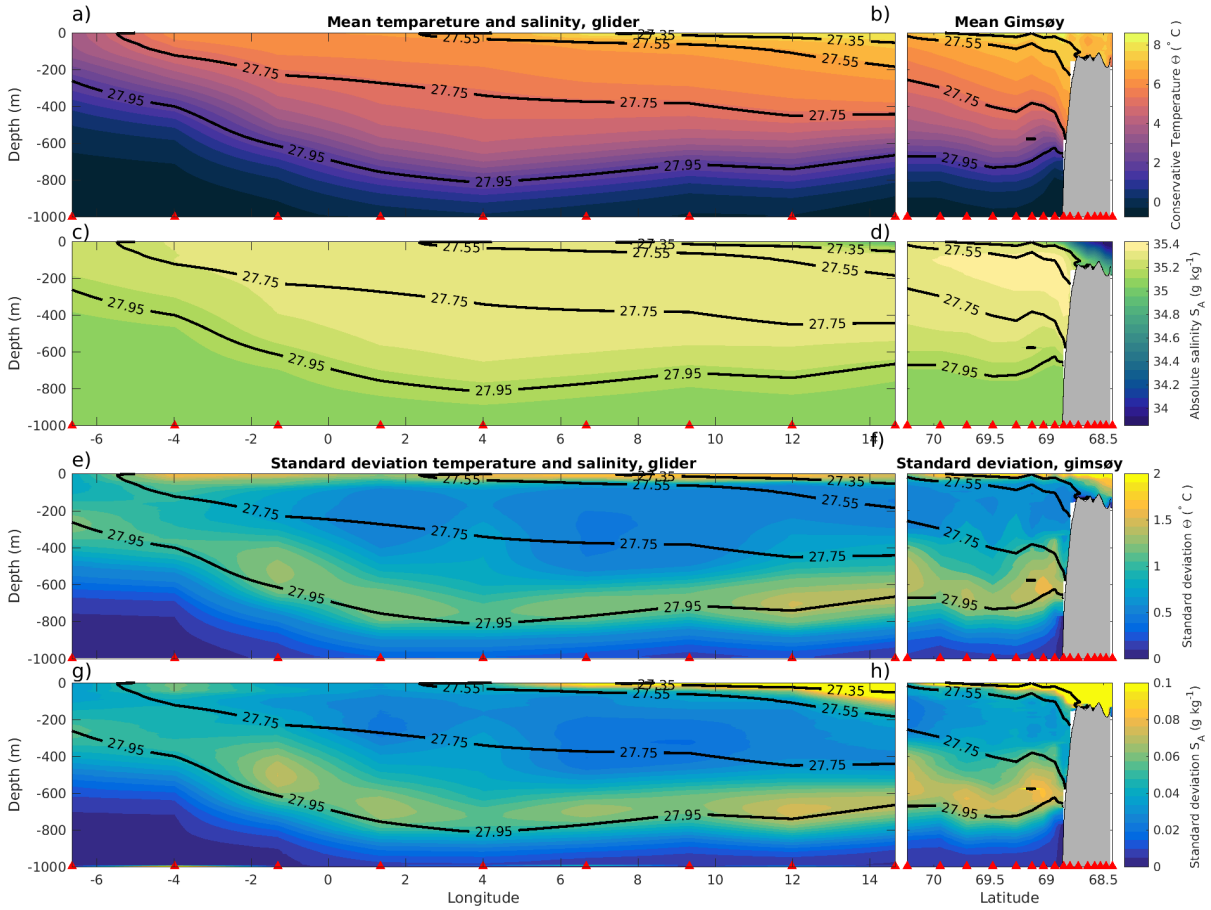

Figure 4.2 – **a)** A zonal section of mean temperature across the LB obtained from glider data. **b)** Mean temperature along the Gimsøy section. **c)** Mean salinity across the LB from glider data. **d)** Mean salinity of the Gimsøy section **e)** Standard deviation of temperature profiles taken by glider in the LB. **f)** Standard deviation temperature for ctd stations in the Gimsøy section **g)** Standard deviation for salinity from glider profiles in the LB **h)** Standard deviation of salinity from ctd stations along the Gimsøy section. In all figures black contours lines show selected isopycnals and y-axis depth. The x-axis for the glider section show longitude and x-axis for the gismøy sections latitude.

The deepest layer of warm and saline water is at the center of the basin at around 4°E. The signature of the LBE is removed by excluding all profiles with temperatures greater then 2.5 °C below 900 m depth. The temperature stays above 5 °C down to about 500 m depth, and the temperature drops down to almost 0 °C over the next 500 m. From the surface and down to 600 m, the salinity is quite homogeneous staying in the range 35.3 - 35.4 g kg^{-1}. Below 600 m, the salinity decreases. West of 4°E, the layer of warm and salty water gets thinner as the transect approaches the edge of the LB. The 27.95 isopycnal sinks toward 4° E from about 250 m on the western edge to 800 m depth. At around 12°E there is a local deepening of warm and salty

water. The isopycnals 27.75, 27.55 and 27.35 are deepest on the eastern edge of the transect, rise towards the surface westward and eventually outcrop.

The Gimsøy section shows that the freshest water (salinity down to $24\,\mathrm{g\,kg^{-1}}$) is located on the shelf. The shelf water is also warm and light, with temperatures around 7 °C and a potential density less than $27.35\,\mathrm{g\,kg^{-1}}$. The isopycnals have a maximum depth toward the shelf where there is a maximum of temperature and salinity. They rise rapidly northward and start sinking again at around 69.1°N, where they sink again reaching a local maximum depth at around 69.7° N, from where they rise toward the surface northward. There is a layer of maximum salinity below the 27.55 isopycnal that gets thinner northward. The temperature roughly follows the same pattern as the salinity. This gives two maximum depths of warm and saline water, one at the slope and another less pronounced at one 69.7° N, from where the layer thins northward. The 27.95 isopycnal follows the same pattern, but does not rise as steeply northward. While shallower isopycnals slope upward with distance from the slope, the 27.95 isopycnal dips downard near the surface.

The standard deviation for temperature is largest in the surface both for the glider transects and Gimsøy section, exceeding 2 °C. The standard deviation at the surface decreases westward. For both the Gimsøy section and glider transects, there is a band of high standard deviation above the 27.95 isopycnal. For the glider transects there are two local maxima in this band, one at 1°W and another almost reaching 2 °C, just off the continental slope at 12°E. The Gimsøy section shows three maxima of standard deviation for temperature, just off the slope at 69°N and two smaller maxima at around 69.6°N and in the north end of the section. The Gimsøy section has the largest standard deviation of temperature near surface on the shelf, where the surface band of high variability deepens landward.

The standard deviation for salinity shows roughly the same pattern as for temperature both for the glider transects and the Gimsøy section. One difference is that the standard deviation in the surface band is much higher than for the band in depth, whereas for the temperature the two bands are comparable. Surface band of high standard deviation also reaches deeper than for temperature, especially near the slope. For the glider transect, the standard deviation is higher than $0.1\,\mathrm{g\,kg^{-1}}$ down to below 100 m depth. For the Gimsøy section, the standard deviation exceeds $0.1\,\mathrm{g\,kg^{-1}}$ for the whole depth of the continental shelf in the part of the section that stretches onto the shelf.

4.2 ANATOMY OF AN ANTICYCLONE

In this section I present the steps taken to describe and quantify an anticyclone using Seaglider observations. The example shows the properties of an anticyclone (A1) and the quantified results can be found in Table 4.1. A1 is observed on the east side of the LB (Figure 4.1).

Based on the criteria of a deep layer of warm water, deepening of density contours and an anticyclonic velocity structure, the eddy is located in the data set by visual inspection(section 2.2). In this case, there is a clear anticyclonic structure in depth-averaged currents that coincide

with the deepening of pycnolines and a deep layer of warm water (Figure 4.3).

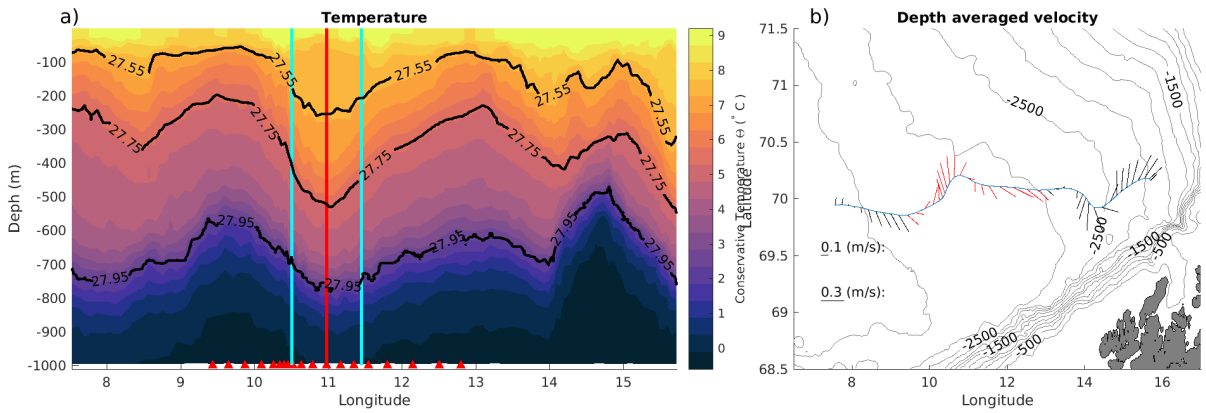

Figure 4.3 – **a)** Distribution of temperature (color) with selected contours of potential density. The vertical red line is at the average longitudinal position of the eddy centers, the blue lines mark the calculated eddy radius. The red arrowheads at the bottom show the position of the profiles that are used in the further analyses of the eddy. **b)** The trajectory of the glider, moving from east to west together with depth-averaged current vectors. The red arrows are used in analysing the eddy. In the bottom left of the figure is the velocity scale at 0.1 and 0.3 m s^{-1}. Topographic contour lines are drawn every 500 m. In the bottom right corner, the Vesterålen islands can be seen.

After a promising candidate has been chosen, eddy centers are calculated for a suitable interval around the index of the profiles in the vicinity of the eddy. The position of eddy centers are detected by using the depth averaged currents to calculate the position of the eddy centers (see section 2.2). It is clear from the velocity structure when a center is good or not. For A1, the velocity structure is clearly anticyclonic around the two detected centers and the temperature at 200 m has a maximum in the vicinity of the centers (Figure 4.4).

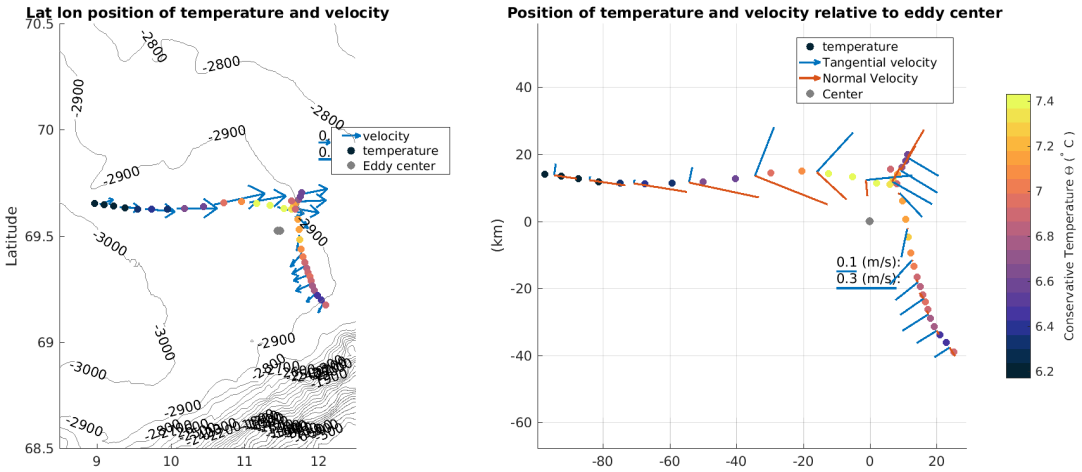

Figure 4.4 – **a)** Temperature at 200 m and the depth-averaged current in geographical coordinates. **b)** Temperature at 200 m and normal and azimuthal velocity vectors relative to the position of the eddy center.

When the centers are selected, the location of the data points are transformed from geo-

graphical coordinates to Cartesian coordinates with the eddy center at the origin. The velocity is decomposed into azimuthal and normal radial components relative to the observed centers. For A1 most of velocities in the vicinity of the center are azimuthal and the structure of an eddy can be seen as the velocity increases from outside toward the center and decay towards the core (Figure 4.4).

To reveal the hydrographic structure of the eddy, the temperature, salinity and density profiles are sorted in bins based on depth and distance from the center. A mean is calculated for every bin and is then smoothed to reduce noise (Figure 4.5). A reference profile for the surroundings is calculated (by taking the mean between the red lines in Figure 4.5) and is used to find isobaric temperature and salinity anomalies.

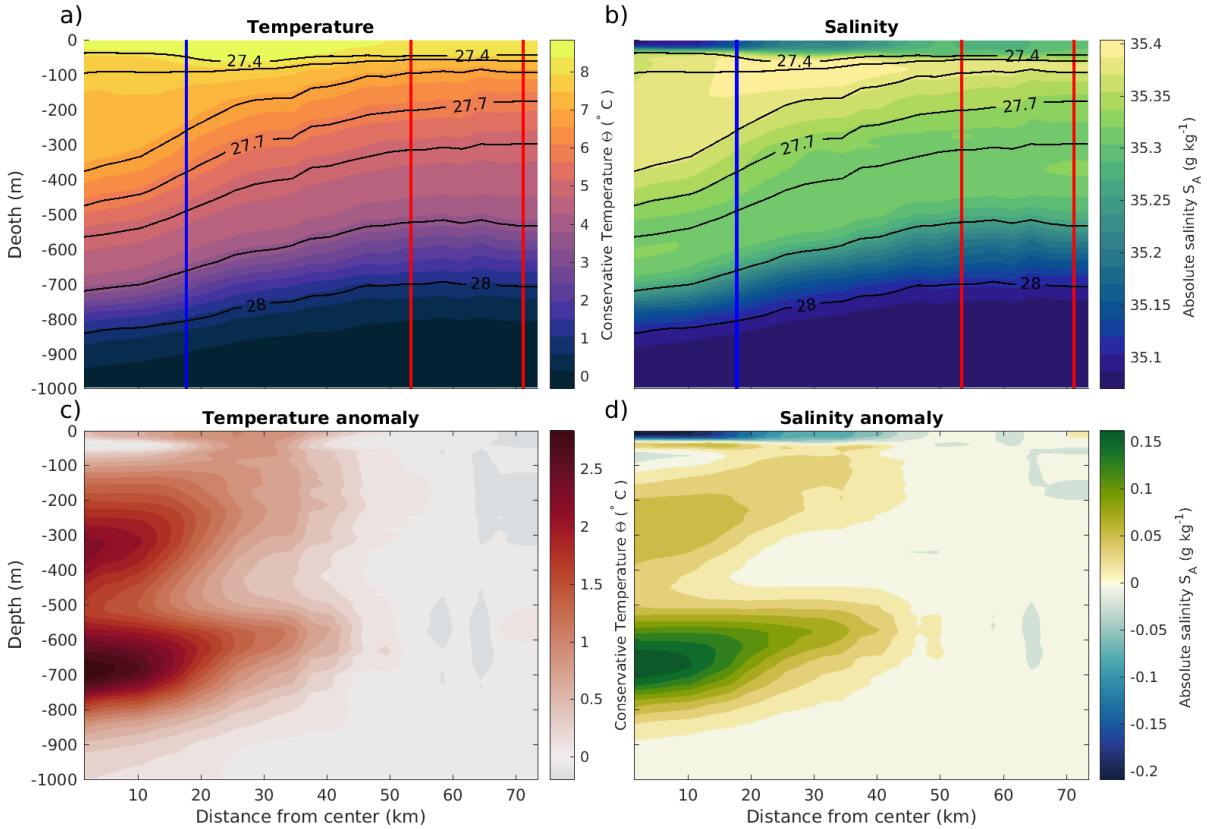

Figure 4.5 – **a)** Binned and smoothed temperature. **b)** Binned and smoothed salinity. The blue line in a) and b) show the eddy radius, R, and red lines, placed at $3R$ and $4R$ show the interval which the mean for the reference profiles is taken over. **c)** temperature anomaly calculated with the reference profile **d)** salinity anomaly. The x and y axis is similar on all plots, the x-axis show distance from center and the y-axis depth.

A1 shows a deepening of the warm and saline layer of water toward the center of the eddy, and the 27.4 and 27.6 isopycnals diverge yielding a layer of homogeneous water. The saltiest water in A1 is in a band at about 100 m depth, and stretches outward for 20 km from the velocity maximum.

In both the temperature and salinity anomaly, there are two areas of positive anomaly with

maximum intensity towards the center. The weakest signal with a maximum temperature and salinity anomaly of approximate 2 °C and 0.05 g kg^{-1} is centered around 250 m depth. The deepest and most intense dome with a maximum temperature and salinity anomaly of approximate 2.7 °C and 0.15 g kg^{-1} is centered around 700 m depth. In the surface there is a strong negative salinity anomaly of maximum 0.2 g kg^{-1} at the center that decreases outwards.

To find a theoretical velocity profile and define the eddy radius (R) the depth-averaged velocities are fitted to a theoretical vortex (section 2.2). The best fit for A1 is a Rankine vortex structure with a depth averaged maximum velocity of 0.34 m s^{-1} at 17.8 km (Figure 4.6 c). The radial distance of the depth-averaged velocity maximum is defined as R, the eddy radius. The geostrophic shear is calculated and combined with the theoretical velocity to find the absolute vortex-velocity down to 1000 m (Figure 4.6 b), the sign of the depth-averaged velocity is corrected to fit with coordinate system.

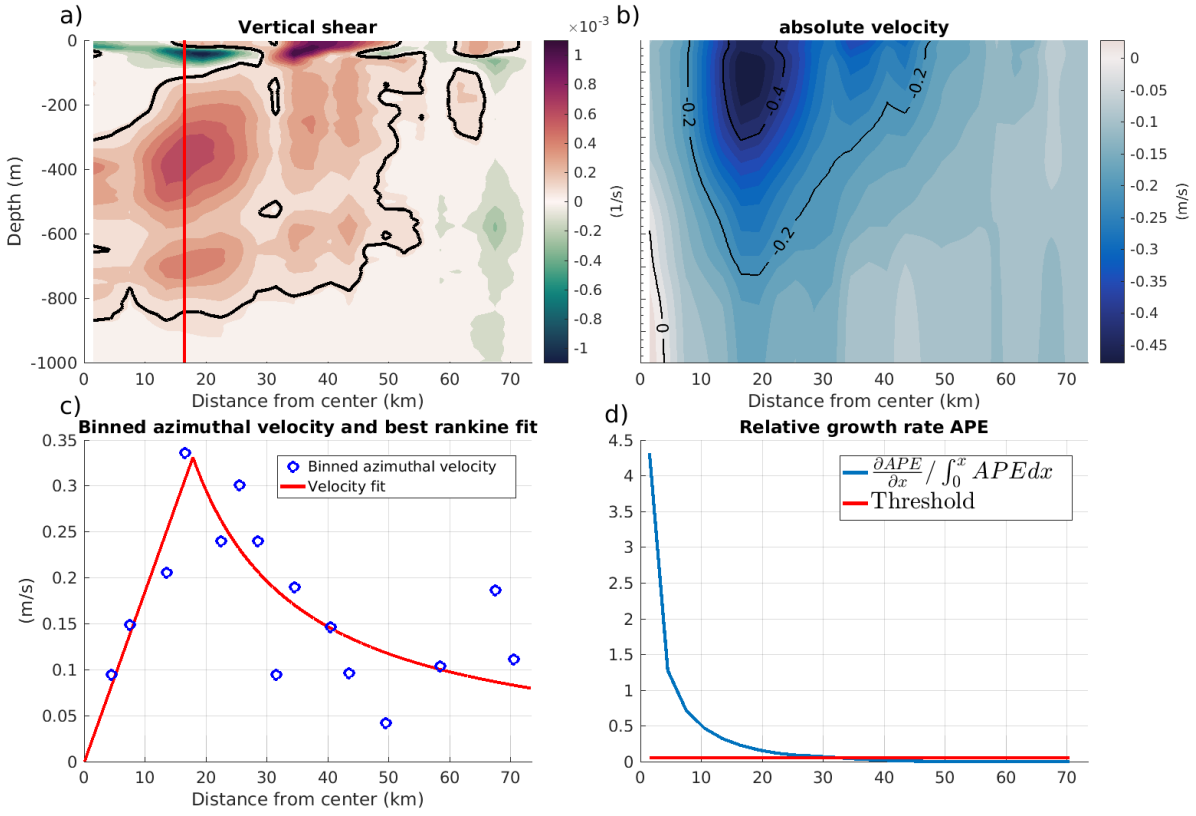

Figure 4.6 – **Radial sections of a)** vertical shear of the eddy velocity, red line show the radial position of maximum velocity and black line the 10^{-4} shear contour. The deepest crossing point of these two gives the eddies depth. **b)** Absolute eddy velocity. **c)** Binned depth-averaged velocity and the best fit for the velocities of a Rankine vortesx. **d)** The relative growth rate of the total amount of APA when integrating outwards and the applied threshold on growth that defines the radial position of R_{di}.

The eddy depth is defined using a threshold on vertical shear, the threshold can be seen in Figure 4.6 a. Another threshold is placed on the radial growth of the total content of APE for

the eddy, which gives a dynamical limit that is used as an horizontal integration limit for eddy energetics (Figure 4.6 d).

A1 has a velocity maximum, v_{max}, at 85 m depth 18 km from the core of $-0.48\,\mathrm{m\,s^{-1}}$. Downwards from the velocity maximum the eddy shear is positive down to 1000 m with a minimum around 400 m. An area with a negative vertical shear is located near the surface in a band stretching from the center to 30 km.

Eddy A1 has an area of low stratification close to its center from about 100 m to 400 meter, and a second area of relatively low stratification stretching outwards in a rising band from 650 m close to the center (Figure 4.7). At the bottom of the eddy the stratification is also weak. The highest stratification is found in the surface layer.

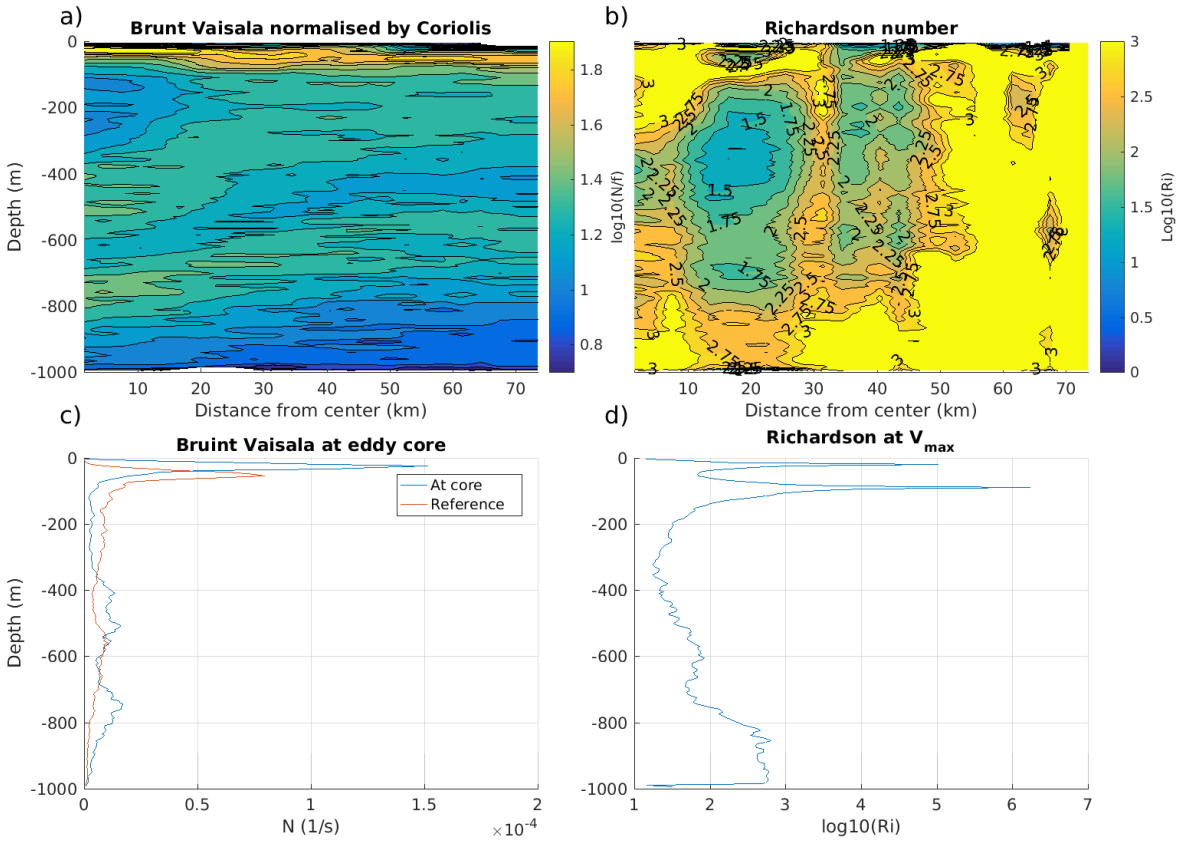

Figure 4.7 – **a)** Buoyancy frequency normalized with the Coriolis frequency on a log scale. **b)** Richardson number on a log scale. **c)** Buoyancy frequency at the eddy core (1.5 km from the center) and the reference profile. **d)** The Richardson number on a log scale at the velocity maximum.

The Richardson number is lowest in an area around 322 m (the depth of Ri_{min}, Table 4.1), slightly outward of the velocity maximum (Figure 4.7 b). This can indicate preferential areas of mixing.

A profile of N^2 at the eddy core shows that highest stratification is at the surface and that the lowest is around 300 m. Compared to the stratification in the reference profile the stratification is greater at the surface for the eddy, and lesser below, down to 400 m. From 400 m and downwards the stratification is generally greater in the core then in the reference profile, except for near

600 m where they coalesce.

4.3 OBSERVED ANTICYCLONE PROPERTIES

In total, 9 anticyclones, from July 28 2012 to May 26 2017, have been characterized, a summary the properties is given in Table 4.1. The values presented are the eddy radius, velocity maximum, the depth of the velocity maximum, the eddy depth, Rossby number(Ro), Burger number (Bu), the minimum Richardson number (Ri_{min}) at the velocity maximum, and the depth of Ri_{min}, the total heat content (HC), salinity content (SC), available potential energy (APE) and eddy kinetic energy (EKE) of the eddy. The mean and std of all the variables for the nine eddies are listed.

All 9 anticyclones were best described by a Rankine vortex, instead of the Rayleigh vortex. The only eddy best described by a Rayleigh vortex was the cyclone, C2.

	A1	A2	A3	A4	A5	A6	A7	A8	A9	Mean
Date	02-Oct-2012	09-Nov-2012	28-Jul-2012	29-Oct-2012	23-Oct-2014	04-Sep-2016	23-Jan-2017	07-May-2017	26-May-2017	-
R (km)	17.8	14.4	17.4	17.7	21.6	18.5	26.3	23.3	10.0	18.6 ± 4.8
Closest profile (km)	3.1	10.1	4.3	3.9	13.1	10.8	0.6	2.7	3.0	5.7 ± 4.4
v_{max} ($m\,s^{-1}$)	-0.48	-0.36	-0.35	-0.24	-0.41	-0.33	-0.46	-0.45	0.32	0.38 ± 0.08
Depth v_{max} (m)	85	210	50	80	110	0	0	95	0	70 ± 68
D (m)	845	1000	955	665	1000	1000	1000	1000	750	913 ± 129
Ro	-0.27	-0.36	-0.11	-0.13	-0.14	-0.19	-0.22	-0.26	-0.29	0.22 ± 0.08
Bu	1.10	1.28	1.69	0.39	1.07	2.61	0.38	0.58	2.15	1.25 ± 0.78
Ri_{min}	17.6	57.3	11.0	55.2	11.2	32.4	0.9	51.7	33.6	30.1 ± 21.2
Depth Ri_{min} (m)	322	858	328	288	422	8	52	832	128	359.7 ± 307.3
10^{18} HC (J)	15.5	8.1	5.0	3.0	31.6	0.8	33.0	27.5	1.8	14.0 ± 13.3
10^{14} SC (gram)	1.4	1.3	0.5	0.3	3.6	0.4	2.9	2.4	0.1	1.4 ± 1.3
10^{13} APE (J)	15.5	5.9	6.1	2.1	27.7	3.5	40.7	30.9	1.0	14.8 ± 14.7
10^{13} EKE (J)	9.3	7.2	1.6	1.7	6.8	6.8	23.9	22.5	1.2	9.0 ± 8.5
R_{di} (km)	34	32	22	28	40	44	44	40	26	34.5 ± 7.9

Table 4.1 – All variables for the characterized anticyclones. Mean is presented with ± std.

4.4 CYCLONES

In addition to the 9 anticyclones, 2 cyclones have been identified and studied, the quantified results are presented in Table 4.2. I will also present the temperature and salinity structure, the depth structure of isobaric anomalies and the absolute velocity for the two cyclones, C1 and C2.

	C1	C2	Mean
Date	04-Feb-2017	02-Jul-2017	-
R (km)	15.5	29.2	22.4
Closest profile (km)	7.1	10.3	8.7
v_{max} ($\mathrm{m\,s^{-1}}$)	0.59	0.44	−0.51
Depth v_{max} (m)	0	0	0
D (m)	1000	1000	1000
Ro	0.23	0.19	0.21
Bu	1.18	0.53	0.85
Ri_{min}	2.8	67.8	35.3
Depth Ri_{min} (m)	17.5	602.5	310.0
10^{18} HC (J)	-3.7	-11.5	−7.6
10^{14} SC (gram)	-0.4	-0.9	−0.6
10^{13} APE (J)	6.1	13.3	9.7
10^{13} EKE (J)	3.6	23.9	13.7
R_{di} (km)	20	38	28.5

Table 4.2 – All variables for the characterized cyclones.

Contrary to the anticyclones, the cyclones have a denser core than the surroundings. When approaching the center the isopycnals rise towards the surface together with a layer of cold and fresh water that has the properties of the deeper layers. For C1, all the density contours rise toward the surface. This is in contrast with C2 where the 27.7 isopycnal and the ones above are seemingly unaffected by the presence of a cyclone, it is only the deeper isopycnals that ascend when approaching the center. In C1 the 27.7 isopycnal makes a small drop downward close to the center (Figure 4.8).

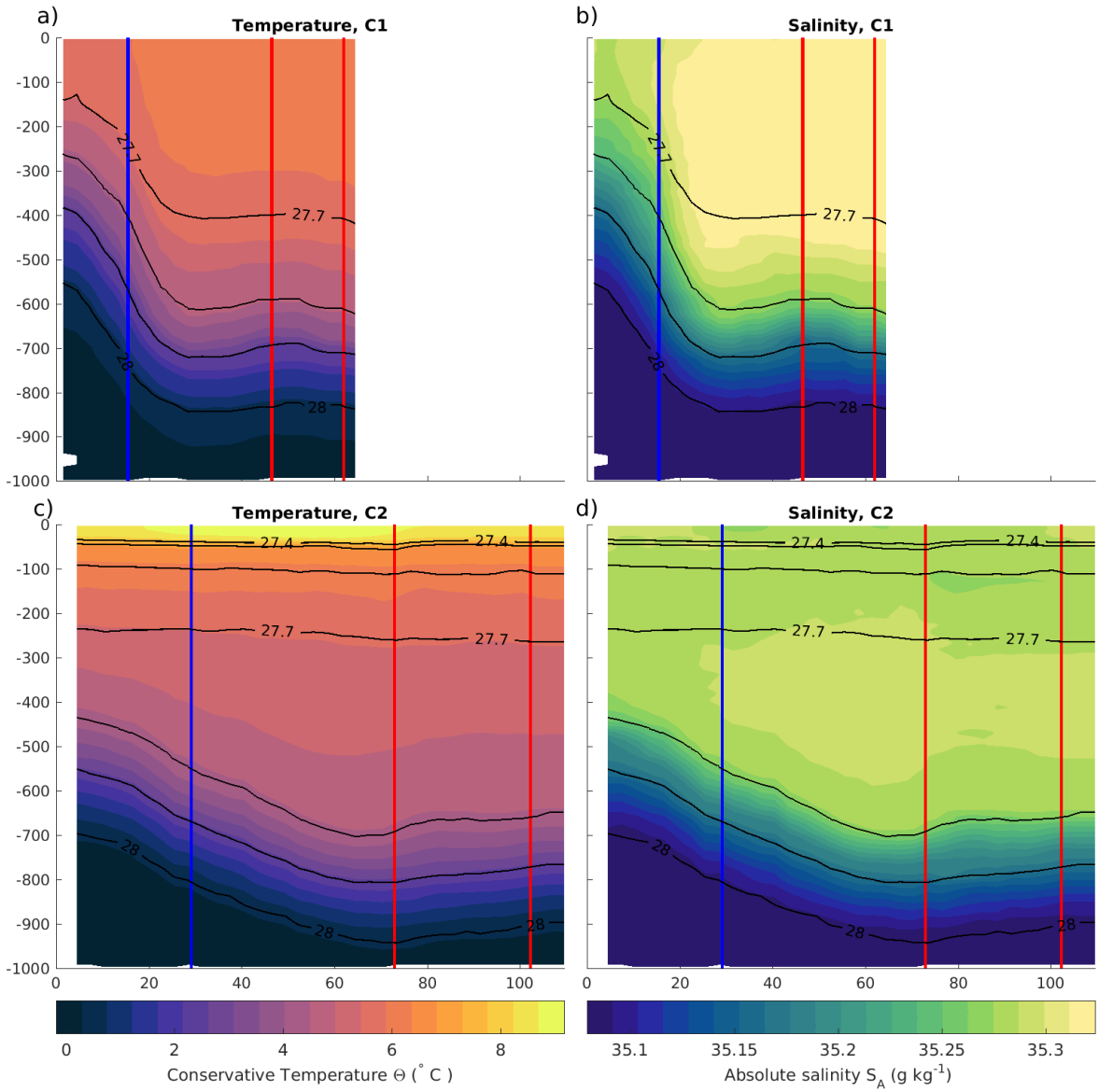

Figure 4.8 – **a)** Temperature c1 1 **b)** Salinity c1 **c)** Temperature c2 **d)** Salinity c2. The blue line show the radial position of the velocity maximum and red lines show the limit of the radial interval used to calculate reference salinity and temperature profiles. x-axis is identical for all plots.

The cyclones have lower heat and salt content than the surrounding water, the total integrated heat and salt content for c1 is respectively -3.7×10^{18} J and -0.6×10^{14} g, for c1 it is -0.4×10^{14} g and -10.4×10^{18} J and -0.8×10^{14} g (Table 4.2). The vertical distribution of the horizontally integrated heat and salt content (Figure 4.9) shows that C1 has a negative content of salt and heat from the surface down to about 800 m where the content fluctuate around 0. For C2, the vertical distribution is different; the heat anomaly is positive down to about 90 m and negative from around 150 m, and most of the heat content is below 500 m depth. The salt content for C2 is negative at surface and positive from around 50 m down to 400 m from where it drops in unison with the heat content with a dual minimum right below 600 and in between 700 and 800 m from 800 m, below which it increases with depth to approx. 0 at 1000 m depth

(Figure 4.9).

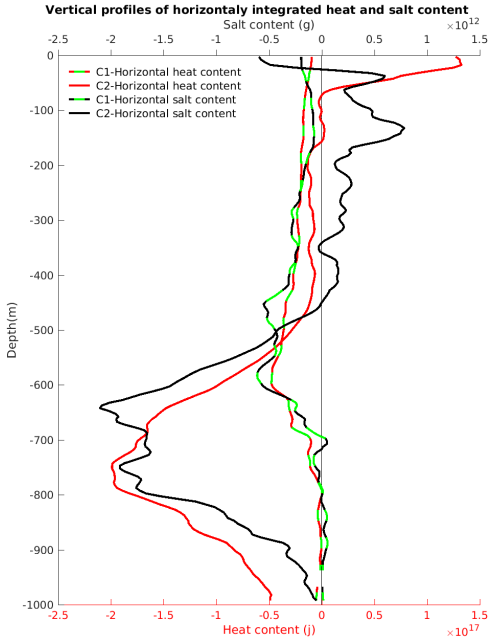

Figure 4.9 – The vertical distribution of horizontally integrated salt and energy content for the quantified cyclones. Partial green lines is cy1 and whole lines cy2. The upper x-axis shows the salt values and is connected to the black lines, lower x-axis show the heat content and is connected to the red lines.

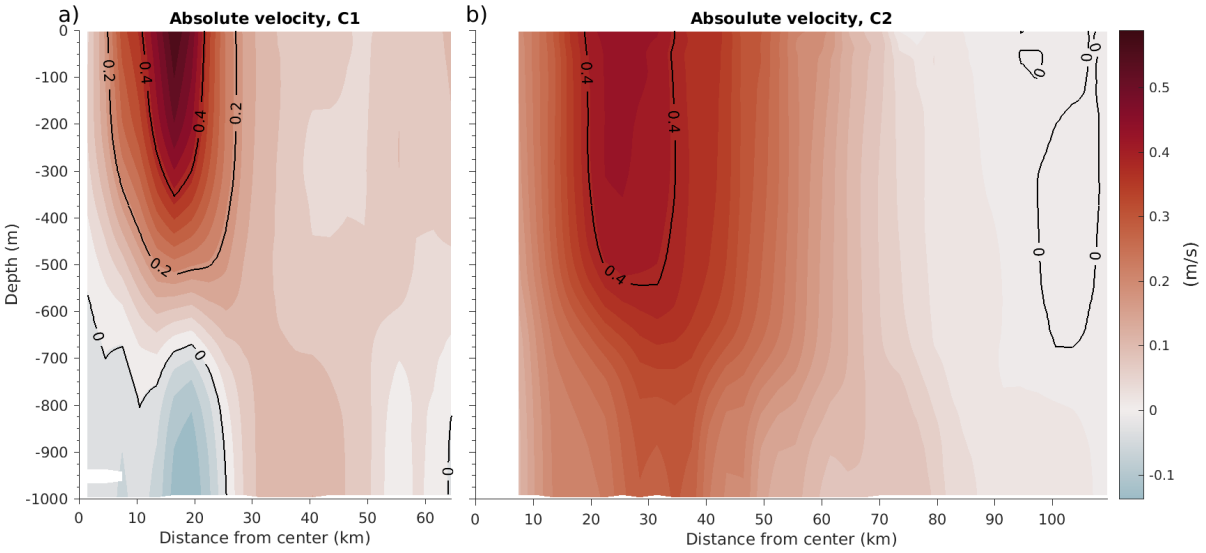

Figure 4.10 – **a)** Radial velocity for c1 **b)** Radial velocity for c2

Both c1 and c2 have v_{max} at the surface and decreasing velocities downward. For c1 v_{max} is $0.59\,\mathrm{m\,s^{-1}}$. At the radial position of v_{max} there is a strong negative shear, causing the velocity to change direction at about 650 m depth, could be that the depth averaged currents are to weak. From about 40 km and outwards the velocity is close to $0\,\mathrm{m\,s^{-1}}$

For C2 $v_{max} = 0.44\,\mathrm{m\,s^{-1}}$, 29.2 km from the center. The velocity maximum has a large vertical extend, from the surface down to 300 m depth, from there the velocity sinks to almost $0.2\,\mathrm{m\,s^{-1}}$ at 1000 m depth. The vertical shear is much weaker for C2 then C1.

4.5 SATELLITE OBSERVED EDDIES

4.5.1 Comparission of glider and satelite observed eddies

Four of the eddies(A5, A7, A8 and C1) characterized from Seaglider observations have simultaneously, or on the day prior, been observed by satellite. Comparison of the glider and satellite observed eddy radius (Table 4.3), show that the radius observed on the same day as the eddies are observed with Seaglider (R_{sat}^{OT}) overestimates the radius with 21, 16, 0 and 12 km compared to the in situ observed radius. Compared to the mean satellite observed radius over the whole observation period numbers are 17.6, 10.9, 15.2 and 16.9 km. Giving a mean overestimation of 15.2 km compared to the mean observed satellite radius and a mean overestimation of 12.3 km on the same day. Giving an overestimation factor of approx. 2.

	R_{glider} (km)	R_{sat}^{OT} (km)	$Mean(R_{sat})$ (km)	$R_{sat}^{OT} - R_{glider}$	$mean(R_{sat}) - R_{glider}$	Lifetime (d)
E5	22	42	39.2 ± 5.3	21	17.6 ± 5.3	71
E7	26	26	37.2 ± 5.6	0	10.9 ± 5.6	47
E8	23	39	38.5 ± 2.5	16	15.2 ± 2.5	35
C1	16	28	32.4 ± 4.9	12	16.9 ± 4.9	35

Table 4.3 – Comparison between eddy radius defined with observed glider velocity observation and satellite deduced radius based on altimeter observed sea level height. The mean satellite observed radius for each eddy is presented with the standard deviation as margin of error.

4.5.2 Geographic location of eddy occurences

The geographic distribution of eddy occurences is shown for both anticyclones and cyclones. An eddy occurence is defined as every daily realization of eddies, an eddy with a 10 day lifetime is counted 10 times, one time for every daily realization. Eddies that are detected for more then 2 consecutive days are included.

Figure 4.11 shows that the highest number of occurrences, both for cyclones and anticyclones are in the center of basin. There is also an area with a large amount of occurrences along the slope. The central area with a high concentration of occurrences can attributed to the permanent LBE and the typical cyclones around it, and does not imply a generation site.

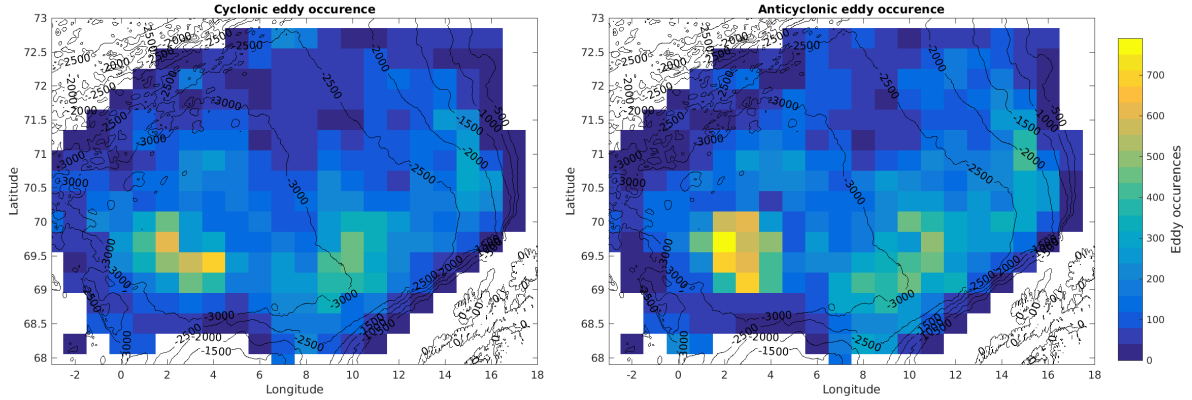

Figure 4.11 – Number of eddy occurrences for cyclones (left) and anticyclones (right). Every day with an observed eddy within the bins are counted as an occurrence.

4.5.3 Geographic distribution of mean Eddy radius

The spatial distribution of satellite-derived eddy radius product show a band of maximum diagonal across the basin. Along the slope the, radius is about 36 km for both anticyclones and cyclones. Sugesting that the radius of eddies is larger in the center of the Basin. The pattern is similar for both cyclones and anticyclones. Eddies with a lifetime of more then 2 consecutive days are included in the statistics.

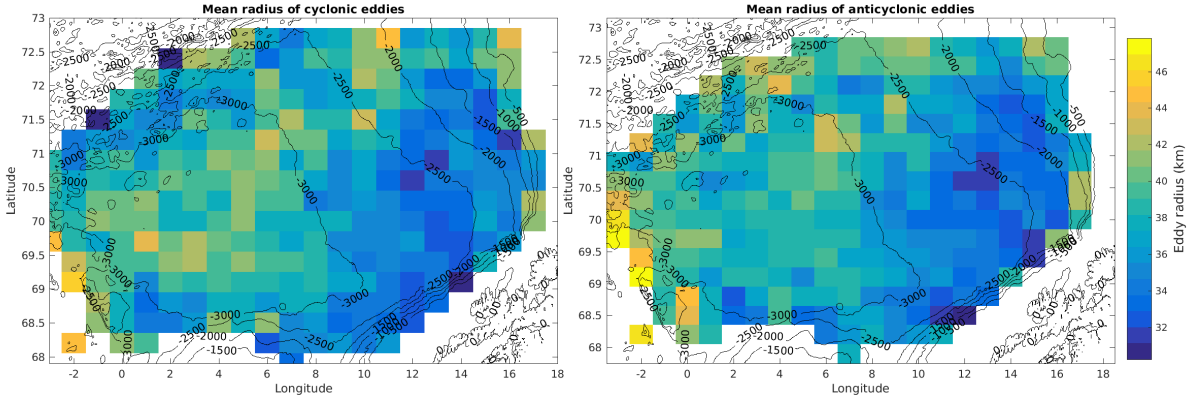

Figure 4.12 – Geographical distrubution of mean eddy radius for cyclones (left) and anticyclones (right).

4.5.4 Locations of eddy generation and mean displacement vectors

Here the geographical distribution of eddy generation and mean displacement vectors for cyclones and anticyclones are shown. An eddy generation is defined as the first position of an unique eddy trajectory. A Displacement vector is defined to go go from the location an eddy is first observed to the last observed location. Only eddies that are observed for more than 5 consecutive days are included.

The areas with the highest generation of anticyclones is off the slope at the eastern part of the basin and in the central part where the LBE is typically located (Figure 4.13).

The mean displacement vector of anticyclones, shows a cyclonic pattern around the center of the basin. Along the slope the eddies move northward and gradually turn westward further north. The pattern converges around the 3000 m isobath from where it goes northward and cyclonical around the basin. On the southern side of the basin, north of the Vøring Plateau, the mean eddy displacement is northward into the center of the basin (Figure 4.13).

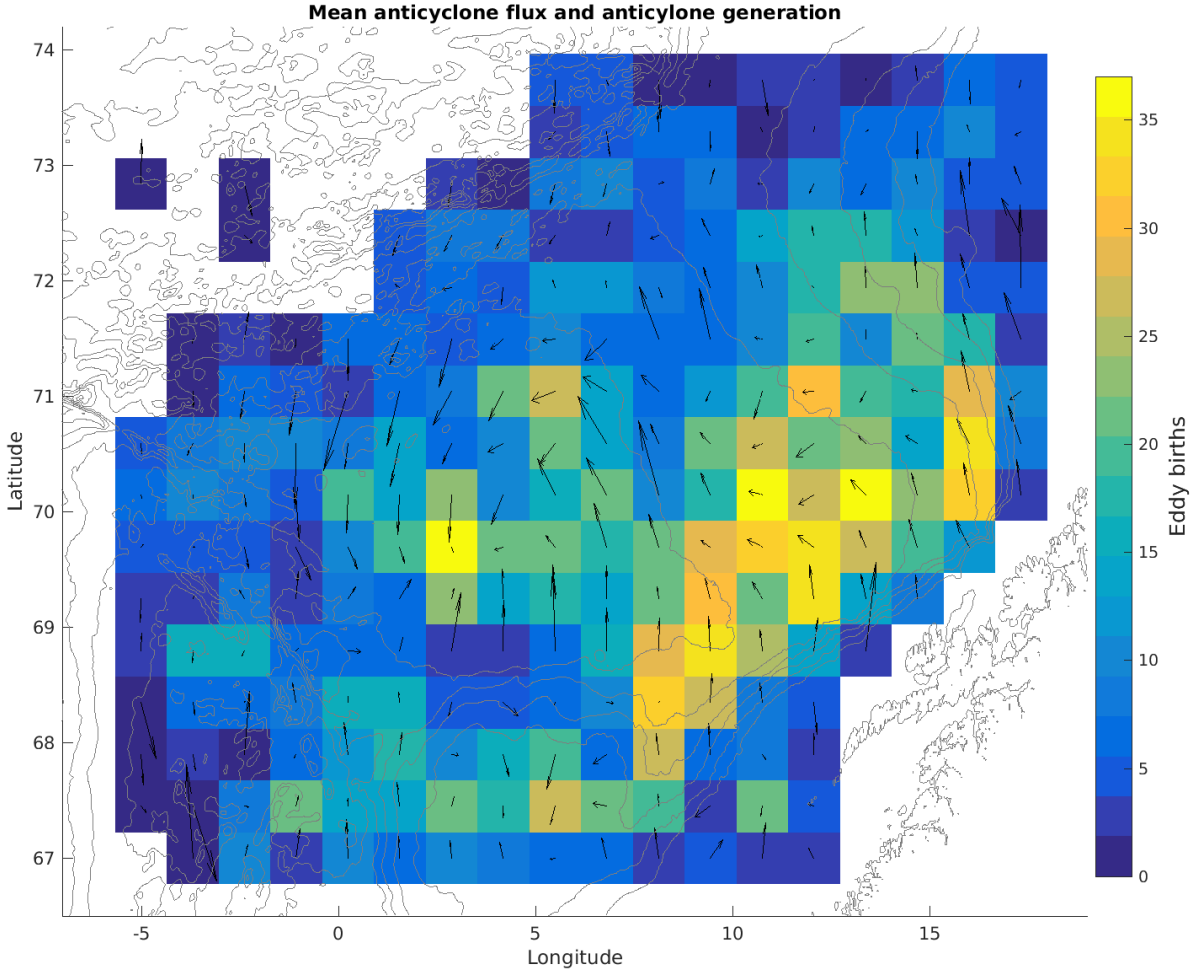

Figure 4.13 – Colormap show the amount of unique anticyclones observed for the first time in each bin. The arrows shows the mean displacement vector for each bin. Only anticyclones observed for more than 6 consecutive days are shown.

The generation of cyclones follow the same pattern as for anticyclones. With a maximum in the center of the basin, near the LBE, and along the slope (Figure 4.14).

The mean displacement vector show the same cyclonic pattern as for anticyclones, But with a cleaner circulation and less tendency to converge towards the center. This is especially clear close to the northern border of the 3000 m isobath, where the anticyclones show a tendency to move towards the center of the basin, while the cyclones propagate strictly westward. On the southern border, the same northward misplacement into the basin as for the Anticyclones is seen.

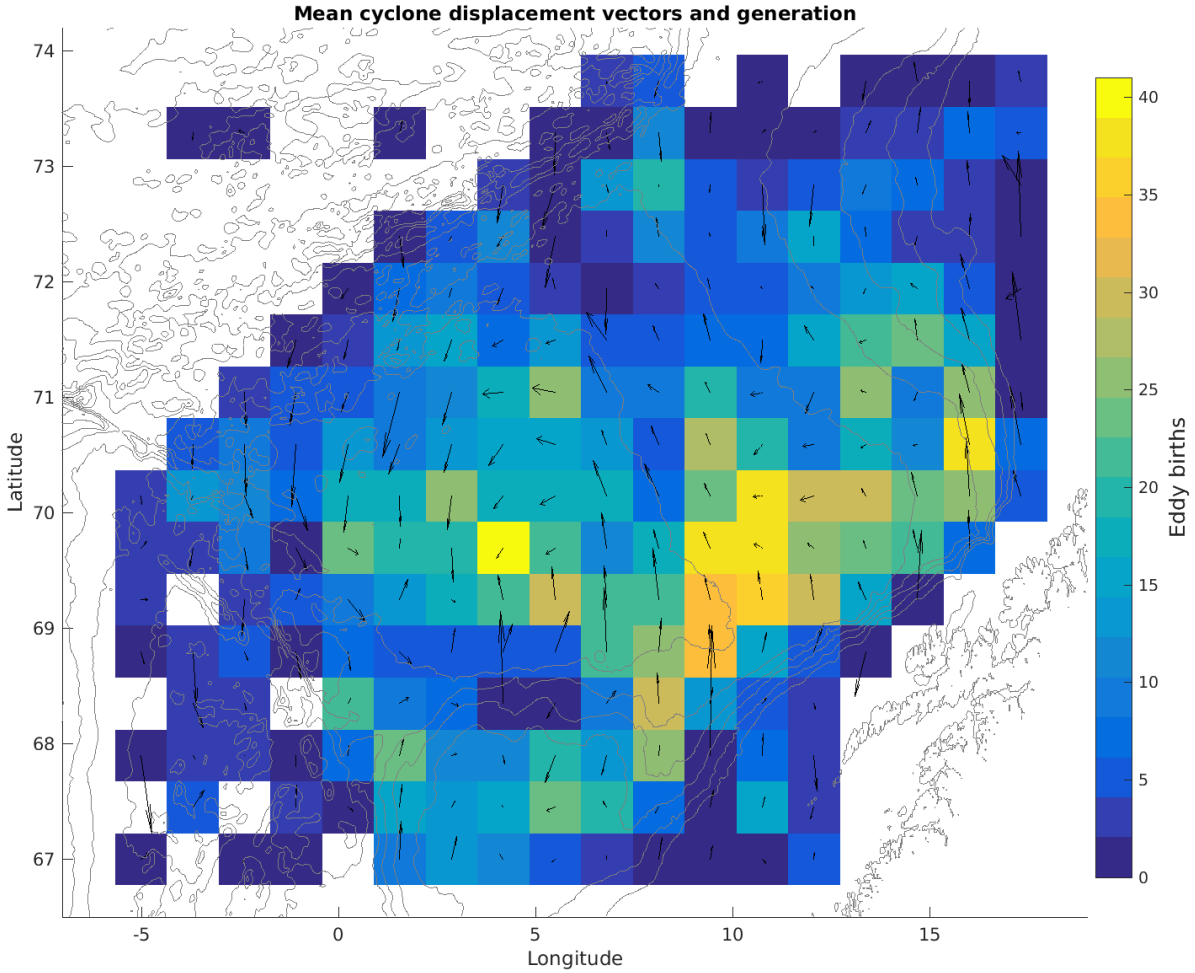

Figure 4.14 – Bins of cyclone generation and mean displacement. Colormap show the amount of unique cyclones observed for the first. The arrows shows the mean displacement vector. Only cyclones observed for more than 6 consecutive days are shown.

5 Discussion

5.1 TEMPORAL VARIABILITY OF OBSERVED EDDIES

Of the nine analyzed anticyclones (AC), only A1, A3, A4, A7, A8 and A9 have profiles close enough to the center to give an accurate representation of the hydrographical properties in the core of the eddy (i.e., the ratio of the radial distance to the center compared to eddy radius is less than 0.3). Of these, three are sampled in 2012 (A1, A3 and A4) and three in 2017 (A7-9). Giving a natural partition in time of well defined ACs observed in 2012 and 2017.

In the time period 2012 to 2017, the LB has experienced a period of freshening, from a salinity maximum in 2011 (*Bosse* et al. 2018). In this section, I discuss the ACs observed in 2012 and 2017 with focus on interannual variability and source waters.

Salinity anomalies and eddy lifetime

Four of the studied ACs were sampled in 2012, all observed by the glider mission M1. Of these ACs, A1, A3 and A4 have a glider profile close enough to the center to get a satisfactory representation of the core, with the closest profiles to the eddy center at 3.1, 4.1 and 3.9 km radial distance, respectively. The properties of the three ACs, are presented in a T-S diagram in Figure 5.2, and as profiles of salinity anomaly at constant pressure surfaces (isobaric anomaly) in Figure 5.1.

Of the three ACs, A1 and A3 have a surface layer that is significantly fresher than the surroundings, by about $-0.2\,\mathrm{g\,kg^{-1}}$ (Figure 5.1). The fresh anomaly at the surface is a typical signature of the shelf waters. The presence of fresh surface water is also an indication that the eddies have not lived through a winter. In winter, the surface cooling would erad-

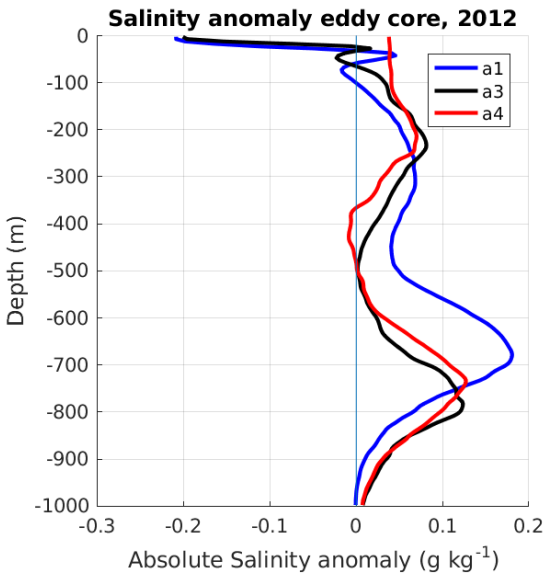

Figure 5.1 – Isobaric salinity anomalies in the center of A1, A3 and A4 observed in 2012. The anomaly is the difference between the salinity of the eddy center and the reference profile calculated for every eddy. Contour lines show potential density.

icate this layer. In winter 2011-2012, *Richards* et al. (2015) found a maximum mixed layer depth of about 200 m in the eastern LB.

All three ACs have a dual isobaric anomaly structure, with one area of anomalies at the eddy core between 200-300m depth, and another larger anomaly further down at the pycnocline. For A1, this deeper layer is at around 650 m depth and for A3 and A4 at 800 m. This is in agreement with the depth of the pycnocline below the AW, (deeper then the seasonal pycnocline at surface) at the location of observation (Figure 4.1). A1 is observed at 11°E and A4 and A3 near 7°E, and the AW pycnocline deepens westward from the continental slope toward the center of the basin at 4°E (Figure 4.2). The high anomaly at depth is a result of depression of the pycnocline by the eddy. This pattern is also reflected in the heat anomalies (not shown).

Source region and T-S properties of the core

5.1.1 Eddies observed in 2012

It is commonly accepted that the ACs are formed in the NwASC. The water from the NwASC is trapped in the eddie, So if it is not transformed, the hydrographic properties will be identical to the source water. Any transformation of the eddies core water will be due to heat or salt loss to the basin, or heat loss to the atmosphere. Warming in summer will only stratify the surface layer, hence cannot change the properties in the interior of the eddy. Therefore, a possible source water will be warmer and saltier or equal to the properties found in the eddy core.

To investigate whether the NwASC is a possible source, the binned profiles closest to the center of the ACs are compared to profiles from the Gimsøy section taken at the continental slope between the 400 - 2000 m isobath, the typical location of the NwASC. I visually inspected all the slope profiles from 2012 taken before the last observed AC, A4 in 29 October 2012. Only one profile from 2012 shows a suitable source (the dark grey line in Figure 5.2). The profile, taken on 5 August, is fresher than the core of both A3 and A4, but it is a reasonable match for A1, assuming that A1 has not been transformed since its formation. The anomalous fresh surface water in A1 is not present in the slope profile, and is likely originated from further towards the shelf, where the water is fresher (Figure 4.2).

None of the sampled realizations of the NwASC in 2012 fulfills the requirements to be a source region for A3 or A4. In 2011 one profile shows the properties that are consistent with a possible source (seen in light grey Figure 5.2). The fresh surface anomaly in A3 indicates that it is formed after the winter mixing ceased. *Richards* et al. (2015) find that the period of restratification in 2012 begins late April, giving a temporal constraint to the formation of A3 towards the end of the mixing period. A3 is observed on 28 July within the 3000 m isobath of the basin (Figure 4.1). If A3 is formed in the beginning of April at the earliest, it has propagated from the slope and into the central part of the basin in a period of 4 months. This is not unrealistic considering that *Richards* et al. (2015) observe a mean eddy propagation of $0.06\,\mathrm{m\,s^{-1}}$. In 4 months, this give a traveled distance of approximately 600 km. The distance from the observation site to the slope is less than half. An eddy propagating with the mean propagation speed, needs approximately

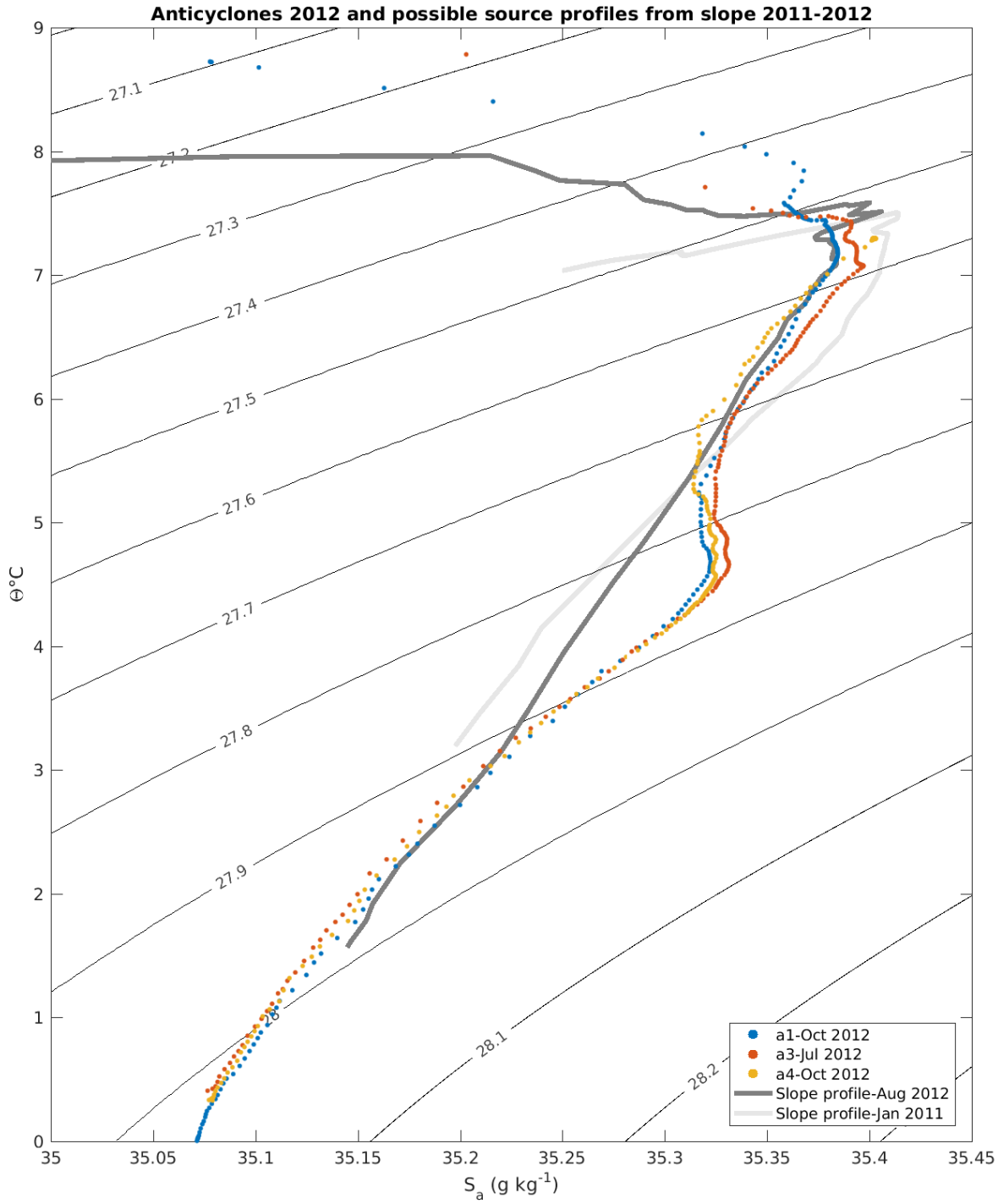

Figure 5.2 – T-S diagram showing the properties of the core profile for A1, A3 and A4 observed in 2012, and selected the CTD profiles from the Gimsøy section. The Gimsøy profiles are from the slope region sampling the NwASC in 2012 and 2011, and are chosen because the T-S characteristics fit with the eddy properties.

2 months to travel from the slope to the observation site, we get another temporal constriction, that A3 is likely formed 2 month prior to observation. Leaving May and April as likely formation months. The fact that A3 is not well described by the slope profiles can be attributed to variations in the NwASC, possibly not captured by the Gimsøy section.

Of the three eddies, A4 has the saltiest and most homogeneous core (seen as the cluster of dots in Figure 5.2). The core extends to the surface. A4 is observed on October 29, close to the observation site of A3 but further west (Figure 4.1). The homogenous core and the positive salt anomaly in the surface, indicates that the eddy has been through a mixing process. This would place the formation time during or prior to winter 2011-2012. One slope profile from 2011 has sampled a potential source for A4 in 2011 (Figure 5.2).

5.1.2 Eddies observed in 2017

The profiles from the three ACs observed 2017 are presented with a T-S diagram in Figure 5.3 and as salinity anomalies on pressure surfaces in Figure 5.4.

Salinity anomaly

Of the characterized eddies observed in 2017 only A9 has an anomalous fresh surface layer (Figure 5.4). With a radius of 10 km, A9 is the smallest of all the characterized eddies. This is reflected in the isobaric salinity anomaly (Figure 5.4). A9 does not depress the AW pycnocline as much as the larger A7 and A8, leading to a weaker salinity anomaly in depth.

A8 has a negative salinity anomaly from the surface, increasing with depth to 200 m before it decreases and reaches nil after 400 m. It is worth mentioning that A8 is observed in a highly variable area, with other cyclones and ACs nearby, so the reference profile may not be perfectly representing the average conditions of the surroundings.

A7 has a stable, slightly positive, salinity anomaly from the surface and down to 200 m depth where it starts to increase. Showing the same structure as A8, maybe indicative of the mixed layer depth in winter 2016-2017.

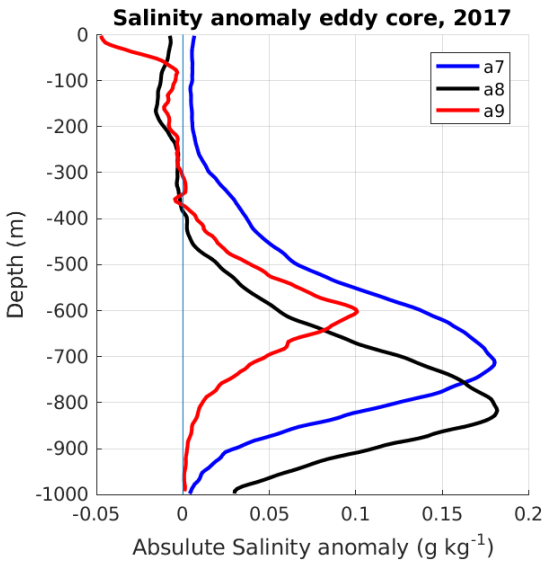

Figure 5.4 – Isobaric salinity anomalies for the center of A7, A8 and A9. The anomaly is relative to the reference profile representing the watermass surrounding the eddies.

Comparison with the slope current and satellite-observed eddy propagation

Since the Gimsøy data analyzed does not extend beyond 2016, the 2017 ACs is only compared to slope profiles from 2016.

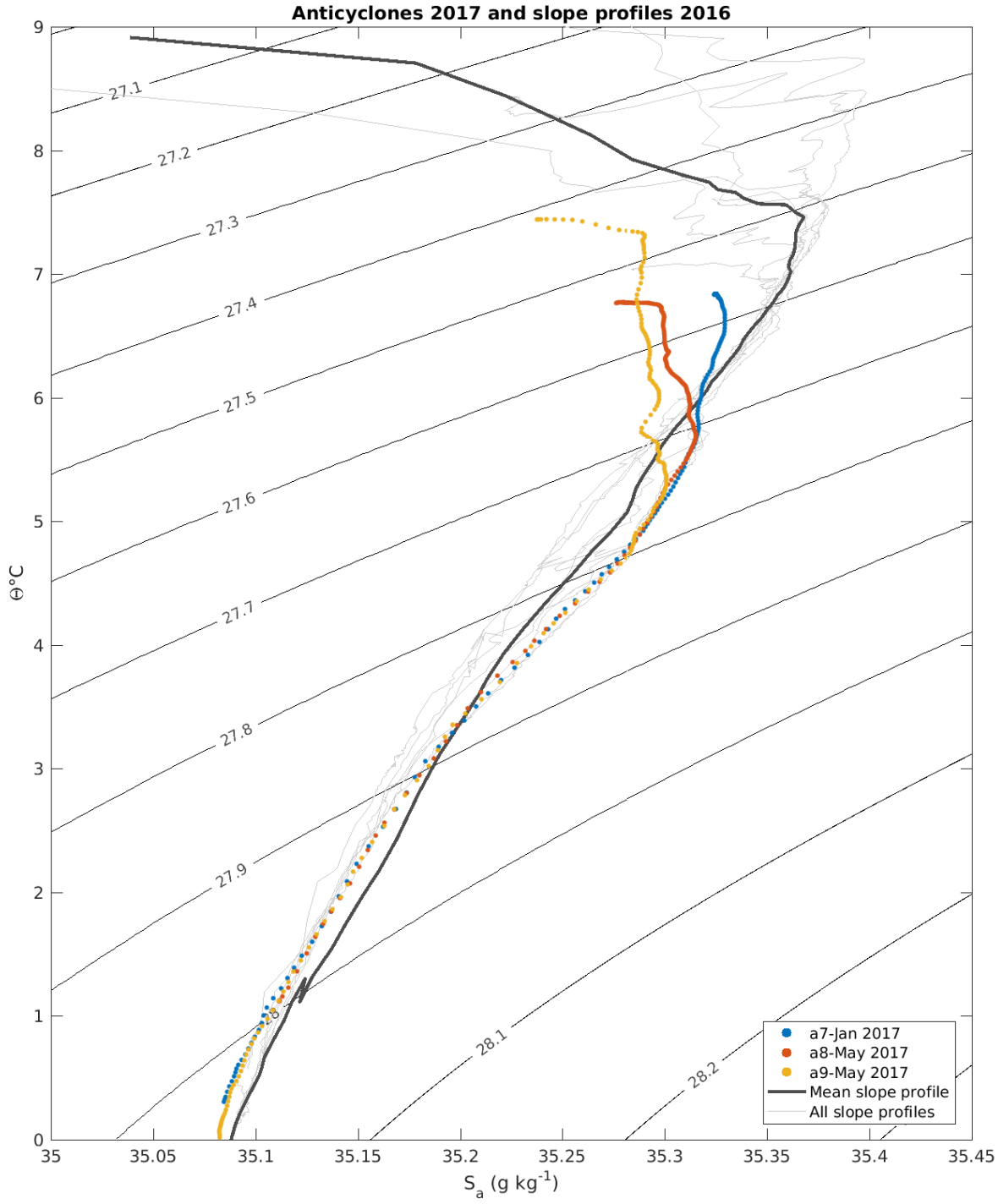

Figure 5.3 – T-S diagram showing the properties of the core profiles for A7, A8 and A9, and all profiles from the gimsøy section taken at slope in 2016 and the mean in thick black line. Contour lines show potential density.

The core properties of A7, A8 and A9 can
be described by almost all the profiles taken at the slope in 2016 (Figure 5.3). But they contain considerable less salt, up to $0.2\,\mathrm{g\,kg^{-1}}$ along isopycnals. This is consistent with the freshening of AW in the basin (*Bosse* et al. 2018).

A7 is observed on 23 January east in the basin, just within the 3000 m isobath. It is the most saline of the 2017 ACs, and therefore has the least discrepancy to the mean 2016 slope profile. It does not have a fresh surface layer relative to its surrounding, or in its hydrographic structure (Figure 5.3). Considering that it was observed in winter, any fresh layer brought from the shelf would quickly be vertically mixed in the eddy.

A7 is observed in the altimetry-derived eddy product. It is first observed on 7 December 2016, southwest of the glider observation site. It showed a meandering north-eastward trajectory (Figure 5.5). The last day the eddy is detected by satellite was 22 January, the day prior to sampling Seaglider. The whole satellite observed trajectory stays within the 3000 m isobath. The displacement vector for A7 does not follow the mean displacement pattern shown in Figure 4.13, but it follows a pattern of cyclonic propagation.

The high salinity and the satellite observation strongly indicate that eddy was formed in 2016. It is both possible that the eddy traveled cyclonic around the basin or that it has been formed at the slope, moved westward, and then started the trajectory observed in the satellite data. Another possibility is that the A7 is formed along the Vøring Plateau and entered the basin from south.

A8 was observed on 7 May, east in the basin, close to the slope. All of the profiles taken at the slope in 2016 are warmer and more saline than the core of the eddy, with the mean slope profile containing about $0.1\,\mathrm{g\,kg^{-1}}$ more salt. If A8 were formed in 2016, it must have lost a large amount of salt to the basin. Considering that the mean properties of the basin are more saline than the eddy (Figure 5.6), this salinity loss is unlikely.

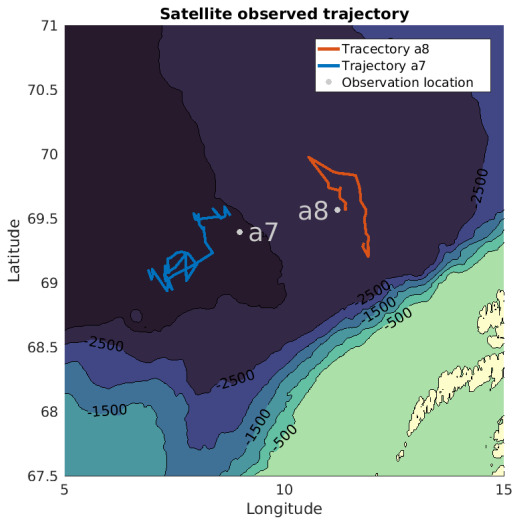

Figure 5.5 – Satelite observed trajectory of A7 and A8

A8 was also observed in the eddy product. It was observed for a total of 35 days, from April 11 to May 15 (temporal limit of the dataset). It is first observed closer to the slope, and has a u-like trajectory to the observation site, first going north then south again to the position where it is observed by the Seaglider on 7 may (Figure 5.5). It stays close to the observation site until the dateset ends. The displacement vector of A8 fits well with the mean displacement pattern (Figure 4.13). The satellite observations of A8 suggest that the eddy is created prior to 11 April 2017 in the NwASC.

Even though the satellite observations suggest that A8 is a newly formed eddy, it does not have the fresh surface layer expected in newly formed ACs. This might be an indication that not all eddies bring with them a fresh surface layer from the slope region, or that the eddy was formed earlier in winter without being detected in the satellite product. The minimum salinity in the surface of A8 is approx. $35.27\,\mathrm{g\,kg^{-1}}$, more saline than the mean salinity of the shelf region. Considering that the standard deviation for salinity on the shelf is greater than $0.1\,\mathrm{g\,kg^{-1}}$ (Figure 4.2), the absence of a fresh layer is not unlikely. The absence of a fresh surface anomaly cannot be used to prove that an eddy has gone trough a mixing process, but the presence of a fresh surface anomaly can indicate that it is has not.

A9 is the freshest of the 2017 ACs (Figure 5.3) and has a fresh surface anomaly. It is observed on 26 May just east of the 3000 m isobath, close to the mean glider trajectory (Figure 4.1). The large discrepancy between the mean profile for 2016 and A9, up to $0.2\,\mathrm{g\,kg^{-1}}$, suggest that it is very unlikely that the eddy was formed in 2016. A9 is most likely formed at the end of or after the mixing season 2016-2017. It is not observed by the satellite eddy product.

5.1.3 Observed freshening of anticyclones

The ACs from 2012 and 2017 is compared to each other and two mean basin profiles centered at 4° and 10°E in a T-S diagram, Figure 5.6. The mean basin profiles are taken over the whole Seaglider sampling period, and the spatial limits are ±1°E around the centers. No limit is set to the north-south extend. The LBE and other cases were the glider dwell in eddies for a prolonged period is excluded.

A comparison of the core profiles of the 2012 and 2017 eddies (Figure 5.6) shows that the eddies from 2012 (A1, A3, A4) are more saline than the eddies from 2017 (A7, A8, A9). All eddies have a layer near the surface with small salinity variations where temperature controls the drop of density. The 2012 eddies have two such layers, one near the surface between the 25.5 and 26.6 isopycnal, and a second one around the 27.8 isopycnal. In contrast, the 2017 eddies show a much deeper layer with a small salinity variation, that stretches approximately from the fresh surface layer and down to the 27.7 isopycnal. The eddies converge as they approach the 28.0 density contour, that is approximate 800 m deep in the center of the basin.

The mean profile in the basin at 10°E lies between the 2012 and 2017 eddies on T-S space (Figure 5.6). Showing that the 2012 eddies are more saline than the mean state around 10°E while the 2017 eddies are fresher. The mean profile at 4°E, that represents the center of the basin where the LBE dominates the eddy variability, shows the same pattern, with the exception of A7 that is saltier upwards from the 27.65 isopycnal than the 4°E mean profile.

Eddy A5 observed in 2014 and A7 observed in 2016 (not shown), fits into this pattern; showing a freshening of eddies with time. The salinity and temperature of the LB are controlled by the influx of eddies shedding from the slope current; it is plausible that the freshening of the basin is due to the observed freshening of the eddies.

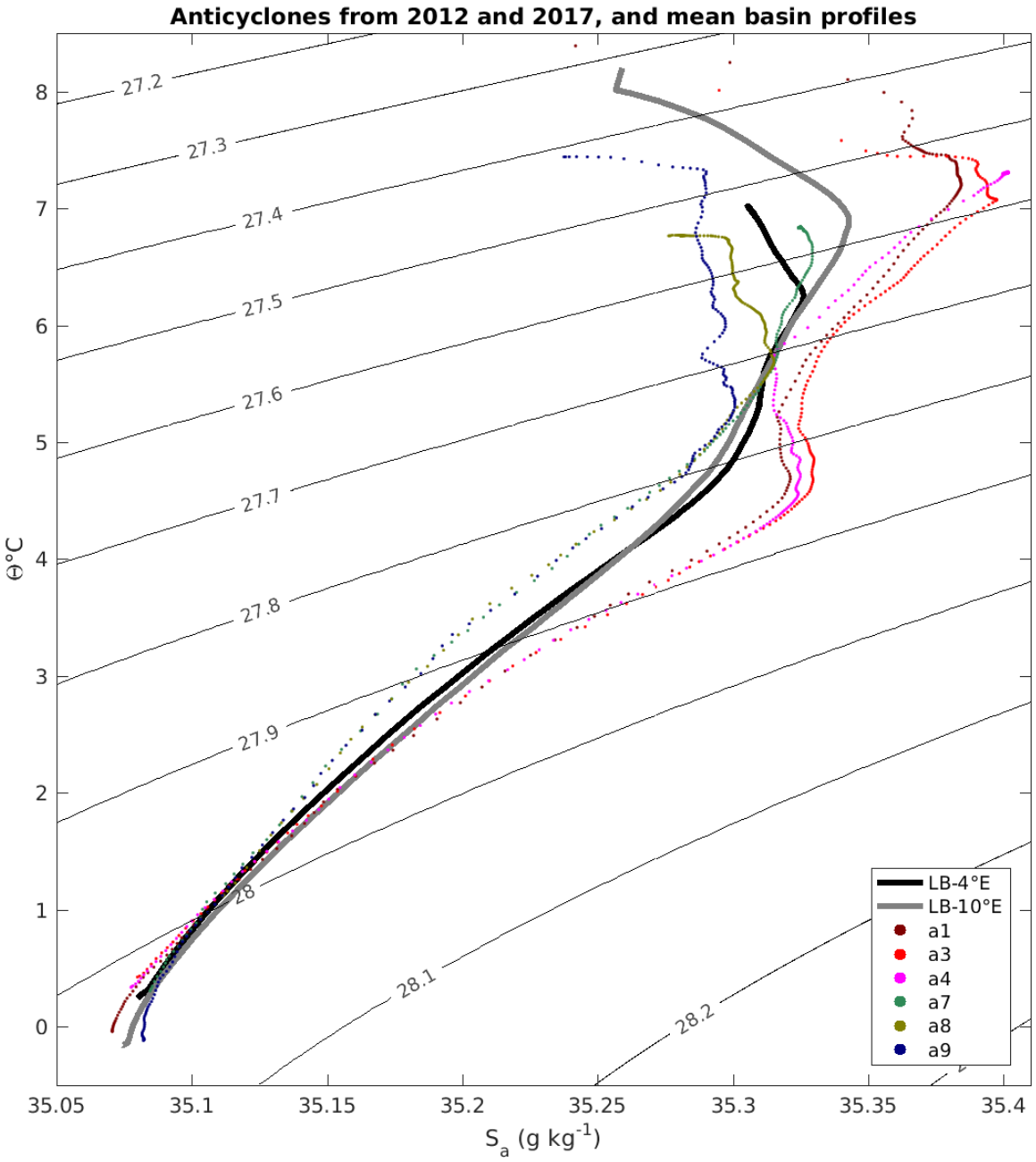

Figure 5.6 – T-S diagram showing the center profile for A1, A3 and A4 from 2012, A7, A8 and A9 from 2017, and mean profiles in the basin centered at 4° and 10° E averaged over the whole sampling period.

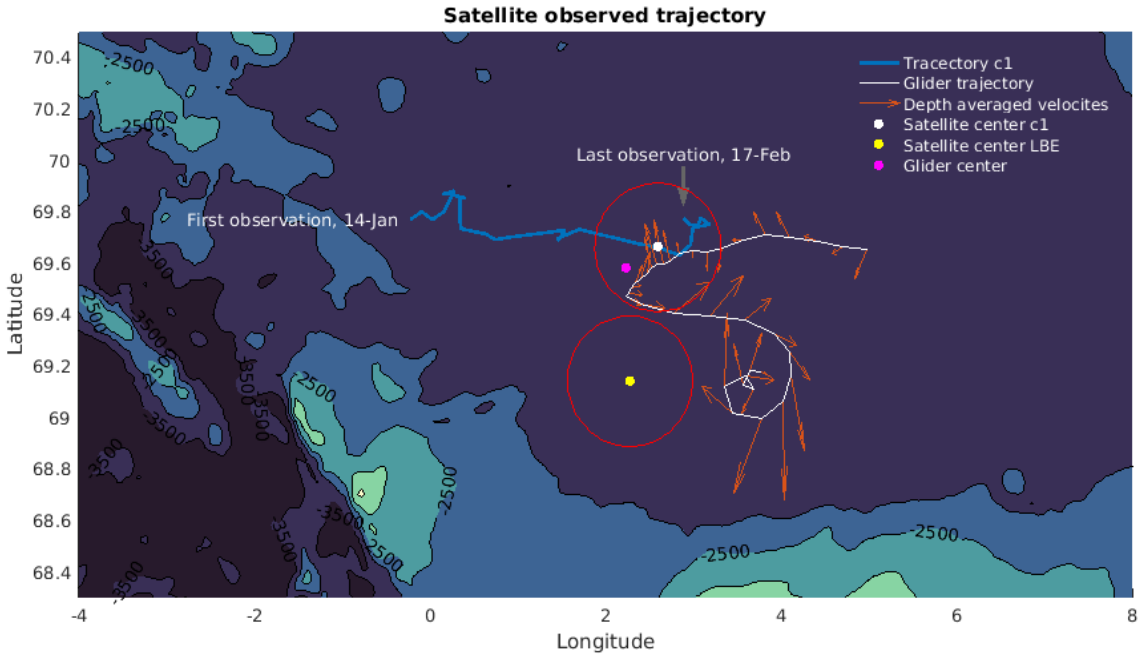

Figure 5.7 – Glider trajectory and depth averaged currents through C1 and into the LBE, satellite-observed position and radius of C1 (white marker) and the LBE (yellow marker), and satellite-observed eastward trajectory of C1. The satellite-observed eddy position and radius is shown for the same day that the center of C1 was observed from glider data. The glider-observed center is shown with pink marker. Satellite observed radius is shown with a red circle around the eddy centers.

5.2 CYCLONES

Two cyclones (CY) have been characterized, C1 and C2, both observed in 2017. In contrast to the ACs they have a negative heat and salt anomaly (Table 4.2).

The reason for the small number of characterized CYs compared to ACs is not only a stronger emphasis on ACs in the study. More CYs could have been characterized from the data set, however, when scrolling through the generated pictures used to locate eddies in the data, there were more pronounced potential ACs than CYs. This might be an indication that the ACs are stronger and clearer than the CYs, and that maybe some of satellite observed CYs are an artifact in the altimetry data due to areas with low SSH in between ACs. But a more systematic approach would be needed to conlude with certainty.

A cyclone interacting with the LBE

C1 is observed deep into the basin at 2.2°E. It is observed close to LBE which the glider enters after passing through the CY (Figure 5.7). The LBE is visible in the strong anticyclonic rotation shown by both the glider trajectory and the depth-averaged velocity. Both the LBE and C1 are observed by satellite. The satellite observation of the LBE is confirmed by water column observations, as the LBE is easily identified in the hydrography by the layer of warm water that stretches down to 1000 m depth (see temperature in Figure 3.2, January, October and December).

In Figure 5.7, the satellite-derived radius and location of C1 and LBE are also shown. The radius and position are from the same day that the Seaglider observed the center of C1.

C1 is located to the north-east of the LBE at the time of observation. When the glider enters the LBE, the LBE has moved eastward since the shown satellite observed location. The glider observed center for C1 is closer to the LBE than the satellite observed center. A mismatch between the in-situ observed dept-averaged velocities and the expected signal of a CY with the satellite observed location and radius is clearly seen. The satellite observed radius is 12.2 km larger than the in situ observed radius, and the distance between the two centers are 16 km.

The deepest part of the basin where C1 is observed is a hot spot of CYs (Figure 4.11). They are most likely linked to the presence of the LBE, which through strong and deep circulation, can spin up CYs. When looking through the generated pictures from the LB, there is a pattern suggesting higher likelihood of CYs in the vicinity of the LBE.

CYs role in the heat content of the basin

According to the satellite observations, CYs are generated in the same locations as ACs (**??**). The mean heat and salt content relative to the surroundings of the observed CYs are -7.6×10^{18} J and -0.6×10^{13} g, while for ACs it is 14.0×10^{18} J and 1.4×10^{13} g. The absolute value of the heat content anomaly is larger for the ACs, with a factor of 2. The statistical presence of CYs within the 2500 m isobath is almost the same as for ACs ((CY occurence)/(AC occurence) = 1.1, for eddies observed longer than 2 days), which indicates that the contribution to the energy content of the upper 1000 m from CYs is approximately one half of that from ACs.

If the CYs are to change the total heat content of the basin, they must be generated outside, and then propagate into the LB. On the west side of the Vøring Plateau, on the border to the Norwegian Basin, there is some generation of CYs in the pathway of the NwAFC. The mean displacement vector indicates that these CYs can propagate into the basin (**??**). The same pattern is seen for ACs (Figure 4.13), so the potential negative heat contribution to the basin from these CYs may be balanced by ACs.

The CYs generated inside the LB do not contain water from a source outside the basin, but colder and fresher waters lifted from deeper layers in the LB. They can have a cooling effect on the layer of AW, but will not diminish the total energy content of the basin. When the cold and fresh water is mixed with the AW layer it will result in fresher and colder water, but also in an expansion of the layer.

5.3 LOFOTEN EDDIES

Characterizations of eddies in the LB based on in-situ observations is few in the literature. Hence these observations makes a step change.

Richards et al. (2015) presented 6 ACs observed from a mooring placed at approximately 7°E, toward the east edge of the 3000 m isobath, and slightly south of the mean glider transect. The ACs were observed between July 3, 2011 and September 5, 2012. The mean velocity over

the upper 500 m were fitted to Rankine vortex, a method similar to the one used here. They found a mean radius of 17.4 ± 9.0 km, comparable to the 18.6 ± 4.8 km mean radius of the AC characterized from Seaglider . They found a mean maximum velocity over the upper 500 m of $0.22 \pm 0.09\,\mathrm{m\,s^{-1}}$, which is comparable but slightly lower than the mean maximum velocity over the upper 1000 m: $0.27 \pm 0.10\,\mathrm{m\,s^{-1}}$ found in this study.

In *Søiland* et al. (2016), 5 realization of the LBE and one AC are characterized. They described the heat content, kinetic energy and potential energy of the AC. Heat content is calculated fitting the mean temperature anomaly over the upper 1500 m to a Gausian curve, and integrating radial to 60 km. To find the total kinetic energy content in the eddy, velocity measured with ship ADCP is integrated vertically down to 500 m depth and horizontally out to 60 km. The total potential energy is found using the dynamic height anomaly, integrated down 1500 m and out to 60 km radius. The methods are comparable to the ones used in this study, but the integration is deeper for hydrographic properties and shallower for kinetic energy.

The heat content of the reported AC is 10×10^{18} J, well within the standard deviation of the mean heat content found for ACs, $14(\pm 12) \times 10^{18}$J. They find a kinetic energy content of 10.0×10^{13} J, within the standard deviation of kinetic energy of ACs found here, $9.0(\pm 8.5) \times 10^{13}$J. The AC closest in radius and velocity to the one observed in the article, A7, have a kinetic energy content of 23.0×10^{13} J. Total potential energy content of the eddy is 1.1×10^{13} J, on the lower end of the mean APE content of ACs found here: $14.8(\pm 14.7) \times 10^{13}$J. The AC in *Søiland* et al. (2016) had a velocity maximum of $0.4\,\mathrm{m\,s^{-1}}$ in the upper few hundred meters and a radius of 27 km, both approximately 50 % longer than the average values obtained here.

When the velocity structure of the eddies is calculated, it has been assumed that they are in a geostrophic balance, and the radial acceleration term in the gradient wind balance (Equation 2.10) has been ignored. The contribution of the nonlinear centrifugal force can estimated by $\frac{V_c}{V_g} \approx 1 - \mathrm{Ro}$,(*Bosse* et al. 2015). The mean Rossby number found is -0.22 ± 0.08 for ACs and 0.21 for CYs. Around 20 % of the velocities in the eddies can be explained by radial forces.

The mean Burger number is 1.25 ± 0.78 for ACs and 0.85 for CYs, which indicates that stratification and rotation effects are of equal importance for the observed eddies.

Richards et al. (2015) found that the velocity signature of eddies goes down to 2500 m, so a large amount of the kinetic energy associated to eddies go deeper than vertical the integration limit down to the eddy depth, of maximum 1000 m, applied here.

For all characterized ACs, depth-averaged velocities for the top 1000 m fit best to a Rankine Vortex. Showing that depth-averaged velocities for ACs are better represented by solid body rotation from the center to the velocity maximum than by velocities corresponding to a Gaussian geopotential anomaly, that is represented by the Rayleigh Vortex.

The smallest CY, c1 ($R = 15.5$ km), fits to a Rankine vortex and the largest, c2 ($R = 29.5$ km), to a Rayleigh vortex. Suggesting that for large CYs a Gaussian geopotential anomaly can be a better approximation, while solid body rotation is a more accurate representation of smaller CYs. However, a sample size of only 2 CYs is not enough to make any confident claims.

5.4 UNRESOLVED EDDIES BY ALTIMETRY

The mean Rossby internal radius of deformation in the basin is found using the binned mean of hydrographic profiles from the Gimsøy section at approximately 69.5° N and 69.95° E from:

$$R_i = \frac{\overline{N}H}{f\pi} \tag{5.1}$$

$\overline{N}$ is the mean buoyancy frequency of the water column, f the Coriolis parameter at 70° N and H the height of the water column (*Alenius* et al. 2003). If calculated for the whole depth of the basin, this gives $R_i = 8.8\,\text{km}$. This is in agreement with the approximately 8 km internal Rossby radius found in the LB by *Nurser* et al. (2014), but not with the size of the observed eddies. If R_i is calculated for the upper 1000 m, which is where the eddies are manifested, $R_i = 18.7\,\text{km}$. This is spot on for the observed mean radius for AC: $18.6 \pm 4.8\,\text{km}$. Inclusion of the CYs put the mean eddy radius slightly above R_i caculated for the top 1000 m. Overall, R_i is as a good approximation for the size of eddies in the LB.

The grid size of the altimeter map used to track eddies is $9.5 \times 27.8\,\text{km}$ at 70° N. To be able to draw a connected isoline in SSH around the center of the eddy, which is a necessity to detect an eddy, at least 9 grid points are needed. One central grid, surrounded by 8 grids with higher or lower SSH. Equaling a block sized $27.8 \times 83.4\,\text{km}$. If we assume that the radius of eddies in the LB is normally distributed around R_i calculated for the upper 1000 m, the minimum size of the block required to draw a connected isoline around an eddy is too large to capture the full picture of eddy activity using satellite altimetry.

This is supported by the fact that only 4 of the total 10 analysed eddies inside the timeframe of the dataset, are observed by the Satellite altimetry-derived product. The observed ACs is the three largest, all with a radius over 20 km. The CY is smaller, with a radius of 15.5 km. So it can not be expected that the full picture of eddy activity is captured. But the eddy statics, and information attained for individual eddies are believed to be valuable.

To characterize the LBE, *Yu* et al. (2017) used the same algorithm and altimetry data used in the eddy product. They found that the satellite observed radius is overestimated by a factor of 2 compared to in-situ Seaglider obervations. This is comparable to my findings (Table 4.3), where the overestimation of eddy radius is of approximate the same size.

5.5 THE BASIN HEAT BALANCE

The average surface heat flux from the LB to the atmosphere averaged over a year is estimated to be $80\,\text{W}\,\text{m}^{-2}$ by *Richards* et al. (2015) and $60\,\text{W}\,\text{m}^{-2}$ by *Isachsen* et al. (2007). The heat loss found by *Richards* et al. (2015) is from in-situ measurements within the 3000 m isobath where the AW layer is the deepest, so it might give an excessive heat loss if applied for the whole extend of the basin.

I define the LB to follow the 2500 m isobath around the basin, and to go in a straight line across the deeper trench on the border to the Norwegian Basin. This gives the LB a surface

area of approximately $2.0 \times 10^{11}\,\mathrm{m}^2$. Multiplying the yearly average heat loss with the area of the basin and numbers of seconds in a year gives a mean yearly heat loss from the basin to the atmosphere of $5.2 \times 10^{20}\,\mathrm{J}$ (for a heat loss of $80\,\mathrm{W\,m^{-2}}$). If this heat loss is to be balanced by an influx of eddies with a mean heat content of $14.0 \times 10^{18}\,\mathrm{J}$, 37 ACs per year will be required. For a heat loss of $60\,\mathrm{W\,m^{-2}}$, 28 ACs per year is required, close to the 25 ACs per year, roughly estimated by *Rossby* et al. (2009).

In an attempt to estimate the number of eddies that enter and deposit their heat in the central part of the basin, I defined a box that roughly follows the 3000 m isobath, and checked how many satellite-observed ACs enters and leave the box. The minimum lifetime of detected eddies is set to 3 days. This gives 230 ACs entering the box and 184 ACs leaving the box, for a sum of 46 ACs entering the interior of the basin over a time period of 24 yr, giving 2 eddies per year. This is not enough to balance the heat loss in the central part of the basin. The reason for this low number is most likely that the algorithm does not detect and track small eddies very well.

The number of ACs required to enter the basin per year to maintain the heat content of the LB is estimated to be between 25 and 37. If we assume that the average lifetime of an AC in the basin is between 3 and 9 months, the mean amount of ACs in the Basin will be between 6 and 28. The mean presence of ACs found by satellite eddy product is 3.4. This number is obtained by dividing every AC occurence inside the 2500 m isobath by the number of days the satellite eddy product covers (eddy lifetime limit is set to 3 days). We also have to consider that a significant portion of the observed ACs is the LBE, which does not bring heat from the NwASC but is a permanent presence in the basin. *Raj* et al. (2015) found the LBE to be present in 80 % of the weekly SSH maps. For the daily SSH maps this portion is likely less, if we assume it is detected 50 % of the time it gives the LBE a mean satellite detected presence of 0.5. The mean presence of ACs originating from the slope is then: 3. Dividing this with the estimated numbers of how many ACs that are in the basin at all time, we get a rough estimate of the portion of ACs that are observed by satellite to be: 0.1 to 0.5. This can also be compared to our study where 3 of 9 ACs were detected by satellite.

5.6 LIMITATIONS OF THE METHOD

Here I discuss weaknesses of the applied method for characterizing eddies from the Seaglider observations.

When detecting the eddy centers the eddies are assumed to be stationary. In the detection algorithm, 4 dives are usually used to locate a center. This corresponds roughly to a period of 24 h. The mean translation speed of eddies is estimated to $0.06\,\mathrm{m\,s^{-1}}$ (*Richards* et al. 2015), and in 24 hours this gives a traveled distance of 5 km, which is a significant fraction of the radius of eddies observed here. This can limit the quality of the observed centers, and can partly explain why for some eddies (these eddies are not included in the study) it was not possible to pinpoint an adequate center.

The eddies are also assumed to be frozen during the sampling period. This could lead to even greater errors due to eddy movement than in the detection of the center, as the dives included in defining the hydrography of the eddy stretches over several days. This also applies for the depth-averaged velocities used to define the theoretical velocity, but the consequences might be limited by the application of a theoretical vortex. The eddies are also assumed to be symmetric, during the process of characterization we observed that this is rarely the case. Observed asymmetries can also be due to eddy translation in the sampling period.

The reference profiles that represent the surrounding water can also be erroneous. The high mesoscale activity in the basin means that other eddies or anomalies can exist in proximity to the observed eddies. Prolonged distances with flat isopycnals which would imply quiescent surroundings are rarely found. As a result, the reference profiles are typically averaged over a larger area, which may not be representative of the surroundings of an eddy.

although a useful tool was defines to detect eddies, combining several pieces of information available, the method is subjective. Eddies are detected manually, furthermore, there can be more eddies that were left uncharacterized in this data set; the analysis was limited a to few well-defined eddies. Finally, the data set is limited to where the glider data were available. Significant portions of the basin with eddies might have been left out because of the lack of sampling.

6 | Conclusion

In this study, mesoscale eddies in the Lofoten Basin have been investigated using hydrographical observations from Seagliders and a satellite altimetry-derived product which tracks and characterizes eddies. Seagliders have proven to be a useful tool for describing the hydrography and, kinematic and dynamic properties of mesoscale eddies. Satellite altimetry and Seagliders work well in tandem. Seagliders can be deployed for long periods collecting a large quantity of data, which makes it a good tool to connect the satellite observed surface signature to the interior of the ocean. A study of this scale and nature would not be economically feasible using ship-based measurements. The joint analysis of the two data sets has been fruitful for studying the mesoscale activity and the heat budget of the basin.

The present study is the most extensive observational study of the eddy field in the Lofoten Basin, hence an important contribution towards understanding the intricate nature of the Lofoten Basin. An average Lofoten anticyclone is found to have a radius comparable to the internal deformation radius. Anticyclones have a positive anomalous heat and salt content while cyclones have an anomalous negative content, smaller by a factor of 2-3. Lofoten eddies are highly energetic (potential and kinetic energy content on order of 10^{13} J and contain significant heat (order of 10^{18} J) and salt anomalies (order of 10^{13} g). Hence they are a significant player in the regional energy budget. Based on the observed heat content of eddies and the mean heat loss from the basin, 28 to 37 anticyclones are required to enter the basin every year.

The slightly nonlinear nature of Lofoten eddies (Rossby number 0.2) help export heat and salt anomalies. The satellite product has been shown to overestimate the radius of eddies and underestimate the amount of eddies in the basin, due to the small radius of the average Lofoten Eddy and the limited resolution in satellite altimetry.

A freshening of anticyclones in the period 2012-2017 is observed. This is in agreement with other studies that have shown a freshening of Lofoten Basin in the same period. This indicates that the eddies originating the Norwegian Atlantic Current controls the salinity and heat content of the basin. The Norwegian Atlantic Slope Current is identified as the main source region for anticyclones.

Bibliography

"Access to products". Copernicus. 2018. http://marine.copernicus.eu/services-portfolio/access-to-products/.

Alenius, Pekka, Alexei Nekrasov, and Kai Myrberg. 2003. "Variability of the baroclinic Rossby radius in the Gulf of Finland". *Continental Shelf Research* 23, no. 6 (): 563–573. ISSN: 0278-4343. doi:10.1016/S0278-4343(03)00004-9. http://www.sciencedirect.com/science/article/pii/S0278434303000049.

Benilov, E. S. 2005. "Stability of a Two-Layer Quasigeostrophic Vortex over Axisymmetric Localized Topography". *Journal of Physical Oceanography* 35, no. 1 (): 123–130. ISSN: 0022-3670. doi:10.1175/JPO-2660.1. https://journals.ametsoc.org/doi/abs/10.1175/JPO-2660.1.

Blindheim, Johan, and Svein Østerhus. 2005. *The Nordic Seas, Main Oceanographic Features*. Vol. 158. doi:10.1029/158GM03.

Bosse, Anthony, et al. 2018. "Atlantic Water Transformation Along Its Poleward Pathway Across the Nordic Seas". *Journal of Geophysical Research: Oceans* 0 (0). ISSN: 2169-9291. doi:10.1029/2018JC014147. https://agupubs.onlinelibrary.wiley.com/doi/abs/10.1029/2018JC014147.

Bosse, Anthony, et al. 2016. "Scales and dynamics of Submesoscale Coherent Vortices formed by deep convection in the northwestern Mediterranean Sea". *Journal of Geophysical Research: Oceans* 121, no. 10 (): 7716–7742. ISSN: 2169-9291. doi:10.1002/2016JC012144. http://onlinelibrary.wiley.com/doi/10.1002/2016JC012144/abstract.

Bosse, Anthony, et al. 2015. "Spreading of Levantine Intermediate Waters by submesoscale coherent vortices in the northwestern Mediterranean Sea as observed with gliders". *Journal of Geophysical Research: Oceans* 120, no. 3 (): 1599–1622. ISSN: 2169-9291. doi:10.1002/2014JC010263. https://agupubs.onlinelibrary.wiley.com/doi/abs/10.1002/2014JC010263.

Carmack, E., et al. 2015. "Toward Quantifying the Increasing Role of Oceanic Heat in Sea Ice Loss in the New Arctic". *Bulletin of the American Meteorological Society* 96, no. 12 (): 2079–2105. ISSN: 0003-0007. doi:10.1175/BAMS-D-13-00177.1. https://journals.ametsoc.org/doi/abs/10.1175/BAMS-D-13-00177.1.

Chafik L. et al. 2015. "On the flow of Atlantic water and temperature anomalies in the Nordic Seas toward the Arctic Ocean". *Journal of Geophysical Research: Oceans* 120, no. 12 (): 7897–7918. ISSN: 2169-9275. doi:10.1002/2015JC011012. https://agupubs.onlinelibrary.wiley.com/doi/full/10.1002/2015JC011012.

Chelton, Dudley B., et al. 2001. "Chapter 1 Satellite Altimetry". In *International Geophysics*, ed. by Lee-Lueng Fu and Anny Cazenave, 69:1–ii. Satellite Altimetry and Earth Sciences. Academic Press. doi:10.1016/S0074-6142(01)80146-7. http://www.sciencedirect.com/science/article/pii/S0074614201801467.

Cushman-Roisin, Benoit, and Jean-Marie Beckers. 2011. *Introduction to Geophysical Fluid Dynamics: Physical and Numerical Aspects*. Academic Press. ISBN: 978-0-08-091678-1.

Eriksen, Charles, and Mary Jane Perry. 2009. "The Nurturing of Seagliders by the National Oceanographic Partnership Program". *Oceanography* 22, no. 2 (): 146–157. ISSN: 10428275. doi:10.5670/oceanog.2009.45. https://tos.org/oceanography/article/the-nurturing-of-seagliders-by-the-national-oceanographic-partnership-progr.

Fer, Ilker, and Anthony Bosse. 2017. doi:10.21335/NMDC-UIB.2017-0001.

Fer, Ilker, et al. 2018. "The Dissipation of Kinetic Energy in the Lofoten Basin Eddy". *Journal of Physical Oceanography* 48, no. 6 (): 1299–1316. ISSN: 0022-3670. doi:10.1175/JPO-D-17-0244.1. https://journals.ametsoc.org/doi/abs/10.1175/JPO-D-17-0244.1.

Gascard, Jean-Claude. 2004. "The Norwegian Atlantic Current in the Lofoten basin inferred from hydrological and tracer data (^{129} I) and its interaction with the Norwegian Coastal Current". *Geophysical Research Letters* 31 (1). ISSN: 0094-8276. doi:10.1029/2003GL018303. http://doi.wiley.com/10.1029/2003GL018303.

Halo, I., et al. 2014. "Eddy properties in the Mozambique Channel: A comparison between observations and two numerical ocean circulation models". *Deep Sea Research Part II: Topical Studies in Oceanography*, The Mozambique Channel: Mesoscale Dynamics and Ecosystem Responses, 100 (): 38–53. ISSN: 0967-0645. doi:10.1016/j.dsr2.2013.10.015. http://www.sciencedirect.com/science/article/pii/S0967064513004098.

Halo, Issufo FM. 2012. "The Mozambique Channel eddies: Characteristics and mechanisms of formation". PhD thesis, University of Cape Town.

Hebert, Dave. 1988. "The available potential energy of an isolated feature". *Journal of Geophysical Research: Oceans* 93 (C1): 556–564. ISSN: 2156-2202. doi:10.1029/JC093iC01p00556. https://agupubs.onlinelibrary.wiley.com/doi/abs/10.1029/JC093iC01p00556.

Isachsen, P. E., I. Koszalka, and J. H. LaCasce. 2012. "Observed and modeled surface eddy heat fluxes in the eastern Nordic Seas". *Journal of Geophysical Research: Oceans* 117 (C8): C08020. ISSN: 2156-2202. doi:10.1029/2012JC007935. http://onlinelibrary.wiley.com/doi/10.1029/2012JC007935/abstract.

Isachsen, Pål Erik. 2015. "Baroclinic instability and the mesoscale eddy field around the Lofoten Basin". *Journal of Geophysical Research: Oceans* 120, no. 4 (): 2884–2903. ISSN: 2169-9291. doi:10.1002/2014JC010448. https://agupubs.onlinelibrary.wiley.com/doi/abs/10.1002/2014JC010448.

Isachsen, Pål Erik, Cecilie Mauritzen, and Harald Svendsen. 2007. "Dense water formation in the Nordic Seas diagnosed from sea surface buoyancy fluxes". *Deep Sea Research Part I: Oceanographic Research Papers* 54, no. 1 (): 22–41. ISSN: 0967-0637. doi:10.1016/j.dsr.2006.09.008. http://www.sciencedirect.com/science/article/pii/S0967063706002573.

Isern-Fontanet, Jordi, Emilio García-Ladona, and Jordi Font. 2003. "Identification of Marine Eddies from Altimetric Maps". *Journal of Atmospheric and Oceanic Technology* 20, no. 5 (): 772–778. ISSN: 0739-0572. doi:10.1175/1520-0426(2003)20<772:IOMEFA>2.0.CO;2. http://journals.ametsoc.org/doi/abs/10.1175/1520-0426(2003)20%3C772:IOMEFA%3E2.0.CO;2.

Jakobsen Philip K. et al. 2003. "Near-surface circulation in the northern North Atlantic as inferred from Lagrangian drifters: Variability from the mesoscale to interannual". *Journal of Geophysical Research: Oceans* 108 (C8). ISSN: 0148-0227. doi:10.1029/2002JC001554. https://agupubs.onlinelibrary.wiley.com/doi/full/10.1029/2002JC001554.

Köhl, Armin. 2007. "Generation and Stability of a Quasi-Permanent Vortex in the Lofoten Basin". *Journal of Physical Oceanography* 37, no. 11 (): 2637–2651. ISSN: 0022-3670. doi:10.1175/2007JPO3694.1. http://journals.ametsoc.org/doi/abs/10.1175/2007JPO3694.1.

Koszalka, I., et al. 2011. "Surface circulation in the Nordic Seas from clustered drifters". *Deep Sea Research Part I: Oceanographic Research Papers* 58, no. 4 (): 468–485. ISSN: 0967-0637. doi:10.1016/j.dsr.2011.01.007. http://www.sciencedirect.com/science/article/pii/S0967063711000306.

McDougall, T.J., and P.M Barker. 2011. *Getting started with TEOS-10 and the Gibbs Seawater (GSW) Oceanographic Toolbox*. http://www.teos-10.org/pubs/Getting_Started.pdf.

Mork, K. A., and Ø. Skagseth. 2010. "A quantitative description of the Norwegian Atlantic Current by combining altimetry and hydrography". *Ocean Sci.* 6, no. 4 (): 901–911. ISSN: 1812-0792. doi:10.5194/os-6-901-2010. https://www.ocean-sci.net/6/901/2010/.

Nurser, A. J. G., and S. Bacon. 2014. "The Rossby radius in the Arctic Ocean". *Ocean Science* 10, no. 6 (): 967–975. ISSN: 1812-0792. doi:10.5194/os-10-967-2014. https://www.ocean-sci.net/10/967/2014/.

Okubo, Akira. 1970. "Horizontal dispersion of floatable particles in the vicinity of velocity singularities such as convergences". *Deep Sea Research and Oceanographic Abstracts* 17, no. 3 (): 445–454. ISSN: 0011-7471. doi:10.1016/0011-7471(70)90059-8. http://www.sciencedirect.com/science/article/pii/0011747170900598.

Orvik, Kjell Arild, and Peter Niiler. 2002. "Major pathways of Atlantic water in the northern North Atlantic and Nordic Seas toward Arctic: MAJOR PATHWAYS OF ATLANTIC WATER". *Geophysical Research Letters* 29, no. 19 (): 2–1–2–4. ISSN: 00948276. doi:10.1029/2002GL015002. http://doi.wiley.com/10.1029/2002GL015002.

Orvik, Kjell Arild, Øystein Skagseth, and Martin Mork. 2001. "Atlantic inflow to the Nordic Seas: current structure and volume fluxes from moored current meters, VM-ADCP and SeaSoar-CTD observations, 1995–1999". *Deep Sea Research Part I: Oceanographic Research Papers* 48, no. 4 (): 937–957. ISSN: 0967-0637. doi:10.1016/S0967-0637(00)00038-8. http://www.sciencedirect.com/science/article/pii/S0967063700000388.

Penven, P., et al. 2005. "Average circulation, seasonal cycle, and mesoscale dynamics of the Peru Current System: A modeling approach". *Journal of Geophysical Research: Oceans* 110 (C10). ISSN: 2156-2202. doi:10.1029/2005JC002945. https://agupubs.onlinelibrary.wiley.com/doi/abs/10.1029/2005JC002945.

Poulain P.-M., Warn-Varnas A., and Niiler P. P. 1996. "Near-surface circulation of the Nordic seas as measured by Lagrangian drifters". *Journal of Geophysical Research: Oceans* 101 (C8): 18237–18258. ISSN: 0148-0227. doi:10.1029/96JC00506. https://agupubs.onlinelibrary.wiley.com/doi/full/10.1029/96JC00506.

Raj, R. P., et al. 2016a. "Quantifying mesoscale eddies in the Lofoten Basin". *Journal of Geophysical Research: Oceans* 121, no. 7 (): 4503–4521. ISSN: 2169-9291. doi:10.1002/2016JC011637. http://onlinelibrary.wiley.com/doi/10.1002/2016JC011637/abstract.

Raj, Roshin P., and Issufo Halo. 2016b. "Monitoring the mesoscale eddies of the Lofoten Basin: importance, progress, and challenges". *International Journal of Remote Sensing* 37, no. 16 (): 3712–3728. ISSN: 0143-1161. doi:10.1080/01431161.2016.1201234. https://doi.org/10.1080/01431161.2016.1201234.

Raj, Roshin P., et al. 2015. "The Lofoten Vortex of the Nordic Seas". *Deep Sea Research Part I: Oceanographic Research Papers* 96 (Supplement C): 1–14. ISSN: 0967-0637. doi:10.1016/j.dsr.2014.10.011. http://www.sciencedirect.com/science/article/pii/S0967063714001940.

Richards, Clark G., and Fiammetta Straneo. 2015. "Observations of Water Mass Transformation and Eddies in the Lofoten Basin of the Nordic Seas". *Journal of Physical Oceanography* 45, no. 6 (): 1735–1756. ISSN: 0022-3670. doi:10.1175/JPO-D-14-0238.1. http://journals.ametsoc.org/doi/abs/10.1175/JPO-D-14-0238.1.

Robinson, Ian S. 2010. "Mesoscale ocean features: Eddies". In *Discovering the Ocean from Space*, 69–114. Springer Praxis Books. Springer, Berlin, Heidelberg. ISBN: 978-3-540-24430-1 978-3-540-68322-3. doi:10.1007/978-3-540-68322-3_3. https://link.springer.com/chapter/10.1007/978-3-540-68322-3_3.

Rossby T., Prater M. D., and Søiland H. 2009. "Pathways of inflow and dispersion of warm waters in the Nordic seas". *Journal of Geophysical Research: Oceans* 114 (C4). ISSN: 0148-

0227. doi:10.1029/2008JC005073. https://agupubs.onlinelibrary.wiley.com/doi/full/10.1029/2008JC005073.

Rossby, C.-G. 1938. "On the Mutual Adjustment of Pressure and Velocity Distributions in Certain Simple Current Systems, II". *Journal of Marine Research* 1, no. 3 (): 239–263. ISSN: 00222402, 15439542. doi:10.1357/002224038806440520. http://openurl.ingenta.com/content/xref?genre=article&issn=0022-2402&volume=1&issue=3&spage=239.

Rossby, T., et al. 2009. "An isopycnal view of the Nordic Seas hydrography with focus on properties of the Lofoten Basin". *Deep Sea Research Part I: Oceanographic Research Papers* 56, no. 11 (): 1955–1971. ISSN: 0967-0637. doi:10.1016/j.dsr.2009.07.005. //www.sciencedirect.com/science/article/pii/S096706370900154X.

Søiland, Chafik L., and Rossby T. 2016. "On the long-term stability of the Lofoten Basin Eddy". *Journal of Geophysical Research: Oceans* 121, no. 7 (): 4438–4449. ISSN: 2169-9275. doi:10.1002/2016JC011726. https://agupubs.onlinelibrary.wiley.com/doi/full/10.1002/2016JC011726.

Talley, Lynne D., et al. 2011. "Chapter 1 - Introduction to Descriptive Physical Oceanography". In *Descriptive Physical Oceanography (Sixth Edition)*, ed. by Lynne D. Talley et al., 1–6. Boston: Academic Press. ISBN: 978-0-7506-4552-2. doi:10.1016/B978-0-7506-4552-2.10001-0. http://www.sciencedirect.com/science/article/pii/B9780750645522100010.

Testor, P., et al. 2010. "Gliders as a Component of Future Observing Systems". In *Proceedings of the "OceanObs'09: Sustained Ocean Observations and Information for Society"*, ed. by J. Hall, D. E. Harrison, and D. Stammer, vol. 2. Venice, Italy: OceanObs'09. http://eprints.uni-kiel.de/10184/.

Voet G. et al. 2010. "The mid-depth circulation of the Nordic Seas derived from profiling float observations". *Tellus A* 62, no. 4 (): 516–529. ISSN: 0280-6495. doi:10.1111/j.1600-0870.2010.00444.x. https://onlinelibrary.wiley.com/doi/full/10.1111/j.1600-0870.2010.00444.x.

Volkov, Denis L., Tatyana V. Belonenko, and Victor R. Foux. 2013. "Puzzling over the dynamics of the Lofoten Basin - a sub-Arctic hot spot of ocean variability". *Geophysical Research Letters* 40, no. 4 (): 738–743. ISSN: 1944-8007. doi:10.1002/grl.50126. http://onlinelibrary.wiley.com/doi/10.1002/grl.50126/abstract.

Volkov, Denis L., Arseny A. Kubryakov, and Rick Lumpkin. 2015. "Formation and variability of the Lofoten basin vortex in a high-resolution ocean model". *Deep Sea Research Part I: Oceanographic Research Papers* 105 (): 142–157. ISSN: 09670637. doi:10.1016/j.dsr.2015.09.001. http://linkinghub.elsevier.com/retrieve/pii/S0967063715001508.

Weiss, John. 1991. "The dynamics of enstrophy transfer in two-dimensional hydrodynamics". *Physica D: Nonlinear Phenomena* 48, no. 2 (): 273–294. ISSN: 0167-2789. doi:10.1016/0167-2789(91)90088-Q. http://www.sciencedirect.com/science/article/pii/016727899190088Q.

Yu, Lu-Sha, et al. 2017. "The Lofoten Basin eddy: Three years of evolution as observed by Seagliders". *Journal of Geophysical Research: Oceans* 122, no. 8 (): 6814–6834. ISSN: 2169-9291. doi:10.1002/2017JC012982. http://onlinelibrary.wiley.com/doi/10.1002/2017JC012982/abstract.

Zhang, Zhengguang, Wei Wang, and Bo Qiu. 2014. "Oceanic mass transport by mesoscale eddies". *Science* 345, no. 6194 (): 322–324. ISSN: 0036-8075, 1095-9203. doi:10.1126/science.1252418. http://science.sciencemag.org/content/345/6194/322.